Turbulent Mixing Processes in Atmospheric Bores and Solitary Waves Deduced from Profiling Systems and Numerical Simulation

STEVEN E. KOCH,* WAYNE FELTZ,+ FRÉDÉRIC FABRY,# MARIUSZ PAGOWSKI,*,@ BART GEERTS,& KRISTOPHER M. BEDKA,+ DAVID O. MILLER,** AND JAMES W. WILSON++

*NOAA/Earth System Research Laboratory, Boulder, Colorado
+ Cooperative Institute for Meteorological Satellite Studies, University of Wisconsin—Madison, Madison, Wisconsin
# McGill University, Montreal, Quebec, Canada
@ Cooperative Institute for Research in the Atmosphere, Colorado State University, Fort Collins, Colorado
& Department of Atmospheric Sciences, University of Wyoming, Laramie, Wyoming
** The Pennsylvania State University, University Park, Pennsylvania
++ National Center for Atmospheric Research,## Boulder, Colorado

(Manuscript received 4 May 2007, in final form 3 August 2007)

ABSTRACT

Families of solitary waves ("solitons") associated with two atmospheric bores on the same day were observed by an unprecedented number of ground-based and airborne profiling systems during the International H_2O Project (IHOP). In addition, a very high-resolution numerical weather prediction model initialized with real data was used with success to simulate one of the bores and the evolving soliton. The predicted wave amplitude, phase speed, wavelength, and structure compared well to these extraordinarily detailed observations. The observations suggest that during the *active phase* (when turbulent mixing was active, which was prior to bore collapse), the bores and waves vigorously mixed dry air from above a nocturnal boundary layer down to the surface. Refractivity computed from near-surface radar observations showed pronounced decreases due to sudden drying during the passage of the bores in this phase, but refractivity *increases* appeared during the period of bore collapse. During both phases, the bores wafted aerosol-laden moist air up to the middle troposphere and weakened the capping inversion, thus reducing inhibition to deep convection development. The model results indicate that the refractivity decreases near the surface were due to drying caused by downward turbulent mixing of air by the wave circulations. Turbulent kinetic energy was generated immediately behind the bore head, then advected rearward and downward by the solitary waves. During the dissipation stage, the lifting by the bore head produced adiabatic cooling aloft and distributed the very moist air near the surface upward through the bore depth, but without any drying due to the absence of vigorous mixing. Thus, this study shows that the moist thermodynamic effects caused by atmospheric bores and solitons strongly depend upon the life cycle of these phenomena.

1. Introduction

One of the coordinated research objectives of the International H_2O Project (IHOP), which occurred from 13 May to 25 June 2002 in the southern Great Plains of the United States, was to seek to improve understanding of the relationship between water vapor and processes occurring in the surface and boundary layers that might have a bearing on convective initiation (Weckwerth et al. 2004). Density currents and bores are lower-tropospheric phenomena that have a proven capability to trigger deep convection (Doviak and Ge 1984; Droegemeier and Wilhelmson 1985; Wilson and Schreiber 1986; Mueller and Carbone 1987; Karyampudi et al. 1995; Koch and Clark 1999). Density currents are primarily horizontal mass flows driven by their greater density relative to their environment. In a stratified atmosphere, a density current may generate a hydraulic jump (a bore), causing a sudden increase in the depth of the layer beneath the inversion (Simpson

The National Center for Atmospheric Research is sponsored by the National Science Foundation.

Corresponding author address: Steven E. Koch, NOAA/ESRL, R/GSD, 325 Broadway, Boulder, CO 80305-3328.
E-mail: steven.koch@noaa.gov

DOI: 10.1175/2007MWR2252.1

1987; Crook 1988; Rottman and Simpson 1989; Haase and Smith 1989a,b). When there is a stable waveguide of sufficient depth at low levels to trap the vertical propagation of wave energy, a bore may evolve into a family of solitary waves known as a "soliton" (Christie et al. 1979; Fulton et al. 1990; Skyllingstad 1991). A solitary wave consists of a single wave of elevation that, owing to a balance between nonlinearity and dispersion, propagates without change of form.

IHOP provided an unprecedented set of data to examine the detailed vertical structure and characteristics of density currents, bores, and solitons, which were observed repeatedly by a large multitude of ground-based and airborne remote sensing systems during the 6-week field phase of IHOP. Of particular interest in this study is to gain an understanding of the mixing processes associated with these phenomena and how this mixing affects the distribution of water vapor and aerosols. Two main types of instability are known for creating turbulent mixing in density currents (Simpson 1987): (i) Kelvin–Helmholtz billows that roll up in the region of speed shear above the head of the current and (ii) lobes and clefts formed by frictional effects on the lower part of the leading edge of the density current. The lobes lead to static instability through an overrunning of the denser fluid in the nose of the current over the lighter fluid. Billows appear to be the primary means by which the air originating from above the inversion is mixed into a density current (Droegemeier and Wilhelmson 1985; Xu 1992; Geerts et al. 2006).

Much less is known about the nature of mixing in atmospheric bores and solitons and how this may impact moisture and aerosol distributions. What little is known comes primarily from laboratory studies, which show that when the depth of the density current (d_b) is greater than the depth of the stable layer (h_0), the flow of the denser fluid within the density current is partially blocked and a bore is generated, which may propagate ahead of it. Mixing processes in bores and solitons increase with the bore strength, defined as the ratio of the mean bore depth to the depth of the inversion layer (d_b/h_0). Laboratory experiments predict that when the bore strength lies in the range of $2 < d_b/h_0 < 4$, mixing commences behind the bore head on the downstream side of the first solitary wave, as well as at points farther downstream where Kelvin–Helmholtz instability may arise (Rottman and Simpson 1989).

An objective of this paper is to compare the remotely sensed and numerically simulated structure of bores and solitons. However, our primary goal is to better understand the nature of the associated mixing processes and how this may impact moisture and aerosol distributions and the convective initiation process. The structure and dynamics of two bores generated during the early morning of 4 June 2002 over the Great Plains provide the basis of this study. Section 2 describes the instruments and analysis techniques used in this study. The design of nested high-resolution model experiments appears in section 3. The results of the multisensor system observational analysis and the model simulations are discussed in sections 4 and 5, respectively. The observed density current, bore, and solitary wave properties are compared to theoretical predictions in section 6. These findings are used in section 7 in the development of a conceptual framework for understanding the nature of entrainment and turbulent mixing processes by the bores and solitons.

2. Instrument description

Measurements of wind, moisture, and temperature with temporal sampling ranging from 1 to 60 min were available during IHOP from a collection of surface mesonetworks (Fig. 1). All of the ground-based remote sensing systems were located at Homestead (HISS), Oklahoma, with the exception of the National Center for Atmospheric Research (NCAR) S-Pol radar, which was located 15 km to the west of Homestead (EAST in Fig. 1). S-Pol is an S-band (2.8 GHz), dual-polarization Doppler radar with 0.91° beamwidth (Lutz et al. 1995). Aside from reflectivity and radial velocity data, S-Pol also provided estimates of the low-level index of refraction up to a range of ~40 km every 5 minutes from the radar following the technique described in Fabry et al. (1997). The refractivity (N) is a function of the atmospheric pressure (P; hPa), the temperature (T; K), and the water vapor pressure (e; hPa), according to Battan (1973):

$$N = 77.6\frac{P}{T} + 3.73 \times 10^5 \frac{e}{T^2}. \quad (1)$$

Thus, the refractivity is a function of a dry density term and a moist term. As air temperature increases, the moist term increasingly dominates over the dry density term. At a temperature of 18°C (representative of the situation herein), a change in N of 10 units (out of a typical range of ~300–350 N units) requires a change of either 10°C in temperature or 2.0 hPa in water vapor (2.0 g kg^{-1} at sea level). Weckwerth et al. (2005) found a very high correlation between S-Pol radar refractivity and that derived from fixed and mobile mesonet observations within a 40-km range of the radar. They also showed that gradients in the S-Pol refractivity field could detect low-level boundaries prior to their appearance in radar reflectivity imagery.

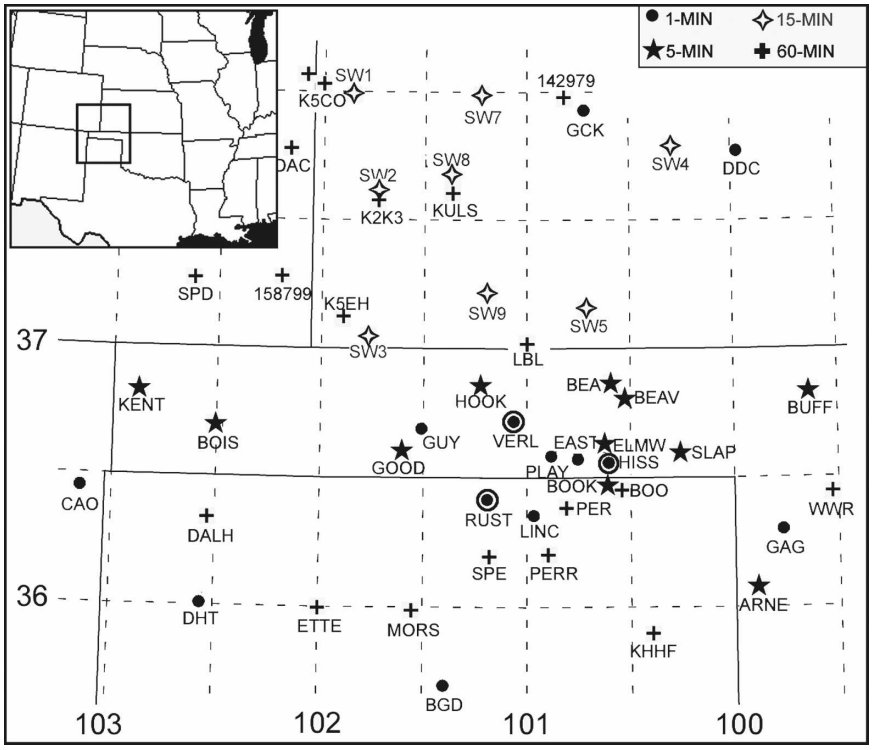

FIG. 1. Surface mesonetwork stations providing data in the region of the Oklahoma Panhandle for this study during IHOP. Dry-bulb temperature, dewpoint temperature, mean sea level pressure, precipitation, and wind speed and direction data were provided by stations using 1- and 5-min sampling resolution. The Southwest Kansas Mesonet (15-min sampling) provided dry-bulb temperature, relative humidity, precipitation, wind speed and direction, wind gust, and radiation values (but no pressure data). Hourly stations provided dry-bulb temperature, dewpoint temperature, mean sea level pressure, precipitation, wind speed and direction, and wind gust data. Time series are shown in Figs. 12 and 13 for the circled 1-min stations. Most of the remote sensing systems, including FM-CW, AERI, SRL, and HARLIE, were located at the Homestead (HISS) facility. The S-Pol radar was located at EAST, which is 15 km west of HISS.

Another system used in this study was the vertically pointing, frequency modulation–continuous wave (FM-CW) radar from the University of Massachusetts (İnce et al. 2003). The chosen FM-CW transmitter frequencies and bandwidth permitted detection of fluctuations in the index of refraction over the lowest 2.5 km of the atmosphere. The high sensitivity of the FM-CW radar to fluctuations as small as a few meters proved to be a valuable resource in this study, though an interference pattern contaminated the lowest 800 m of the returned signal, complicating interpretation of the data.

The NCAR Multiple Antenna Profiler (MAPR) provided measurements of the horizontal and vertical wind components with 30-s time resolution and 60-m height resolution over a depth of ~2.5–4.0 km (Cohn et al. 2001). MAPR was the only system that provided direct and frequent measurements of winds. Five-minute dropouts occurred on the half-hour because of Radio Acoustic Sounding System (RASS) sampling.

Two National Aeronautics and Space Administration (NASA) lidars were used in this study: the Scanning Raman Lidar (SRL; Whiteman et al. 2006a,b) and the Holographic Airborne Rotating Lidar Experiment (HARLIE; Schwemmer et al. 1998). Measurements of aerosol backscatter, cloud optical depth, depolarization, water substance, and temperature were all produced by SRL, but of greatest interest to this study are mixing ratio measurements made with a temporal resolution of 2 min and a vertical resolution that varied from ~30 to 200 m. HARLIE is an aerosol backscatter lidar operating in a conical scanning mode at a 45° elevation angle at a rate of once every 12 s with range resolution of 30 m. By adding all profiles from each scan, backscatter signal displays were produced. Since the values at each altitude are an average of all of the data over all scan angles, the effective altitude resolution of the imagery is actually ~50 m below 2-km altitude, above which it gradually degrades to ~250 m.

Retrieved profiles of temperature and moisture were provided below cloud base every 10 minutes by the Atmospheric Emitted Radiance Interferometer (AERI) from the University of Wisconsin—Madison (Feltz et al. 1998, 2003a,b; Knuteson et al. 2004a,b). A statistical retrieval was combined with hourly Rapid Update Cycle (RUC) model profiles to provide a nominal hybrid first guess of temperature and moisture to the AERI physical retrieval algorithm. AERI downwelling radiance measurements provided temperature and moisture profile corrections in the planetary boundary layer (PBL) below 2.5 km. The AERI data have a vertical resolution of 50 m in the 0–1-km layer, degrading to 250 m in the 2–3-km layers.

The NCAR Integrated Sounding System (ISS) system at Homestead (Cohn et al. 2001) provided detailed soundings every three hours. These data were used to assess the environment associated with the bores and to provide needed measurements to calculate bore properties from theory. The data were subjected to low-pass smoothing and automated quality control to remove suspect data points that did not pass tests for internal and vertical consistency, gross limit checks, and rate-of-change limits for temperature, pressure, and ascension rate.

The final observing system used in this study was a set of in situ measurements (including turbulence) made by the University of Wyoming King Air (UWKA). The UWKA flew along a set of paths directed perpendicular to the bore fronts. The first flight leg flown at 1850 m AGL intercepted one of the bores, while subsequent flight legs were made behind the bore. Pressure perturbations at flight altitude $[p'(t)]$ were calculated using the method of LeMone et al. (1988), wherein the difference between the actual aircraft altitude z_a (calculated as the sum of the radar altitude plus the topographic elevation) and the pressure altitude z_p (derived from the flight-level static pressure and the temperature profile measured by the UWKA assuming hydrostatic balance) was used to determine $p'(t)$ as

$$p'(t) = \rho g[z_a(t) - z_p(t)]. \quad (2)$$

High covariance between the temperature and potential temperature flight-level traces (not shown) implied that the aircraft did not bob up and down with the solitary waves but, rather, that it flew nearly level relative to the ground.

3. Numerical model configuration

Idealized numerical model simulations of density currents, bores, and solitons have added significantly to our understanding of these phenomena (e.g., Droegemeier and Wilhelmson 1985; Crook 1988; Haase and Smith 1989a,b; Xu 1992; Jin et al. 1996), but the ability to numerically predict these phenomena accurately using a numerical weather prediction model initialized with real data has not been fully established. Haase (1991) simulated a borelike disturbance associated with an observed cold front. Manobianco and Nutter (1999) numerically predicted observed density currents in the form of a sea breeze. Thomsen and Smith (2006) simulated a borelike disturbance on a stable layer, which was provided by the relatively cool air associated with a sea breeze. The present study differs from theirs in several important respects: 1) our study employs a model with a resolution several times higher than theirs (0.7 km versus 3.0 km), which made it possible to simulate multiple solitary waves with horizontal wavelengths smaller than 10 km; 2) the current study places a much greater emphasis on verifying the numerical prediction of solitary wave characteristics (horizontal wavelength, wave amplitude, phase speed, and structure) using a large number of remote sensing systems and aircraft data; and 3) the forcing mechanism for the bores in the present case was precipitation, not a sea breeze or topography, which we believe is a far greater challenge for a model to be able to predict correctly.

We performed simulations with a very high resolution version of the fifth-generation Pennsylvania State University–National Center for Atmospheric Research Mesoscale Model (MM5) initialized with real data. The MM5 model was set up in a quadruple nested-grid configuration, beginning with an 18-km resolution domain run initialized at 0000 UTC 4 June 2002 with operational 20-km RUC analysis fields. Three increasingly smaller higher-resolution grids were then established in a one-way nesting configuration at 6.0-, 2.0-, and 0.7-km grid mesh sizes. The three coarser grids used 32 vertically stretched sigma coordinate surfaces, whereas the 0.7-km domain was run with 44 vertical levels, one-half of which were contained below the 1.5 km level to provide high vertical resolution where it was most needed.

The model runs used the Burk and Thompson (1989) PBL scheme, a 2.5-level closure method in which the mixing length is diagnosed. The other physics used in this simulation consisted of the Blackadar surface flux method (Zhang and Anthes 1982), the Grell and Dévényi (2002) ensemble convective parameterization scheme (only for the 18-km grid), the Reisner et al. (1998) mixed-phase microphysics scheme, the RUC land surface model (Smirnova et al. 2000), and the Mlawer et al. (1997) radiation scheme. An experiment was also performed to examine the sensitivity of the

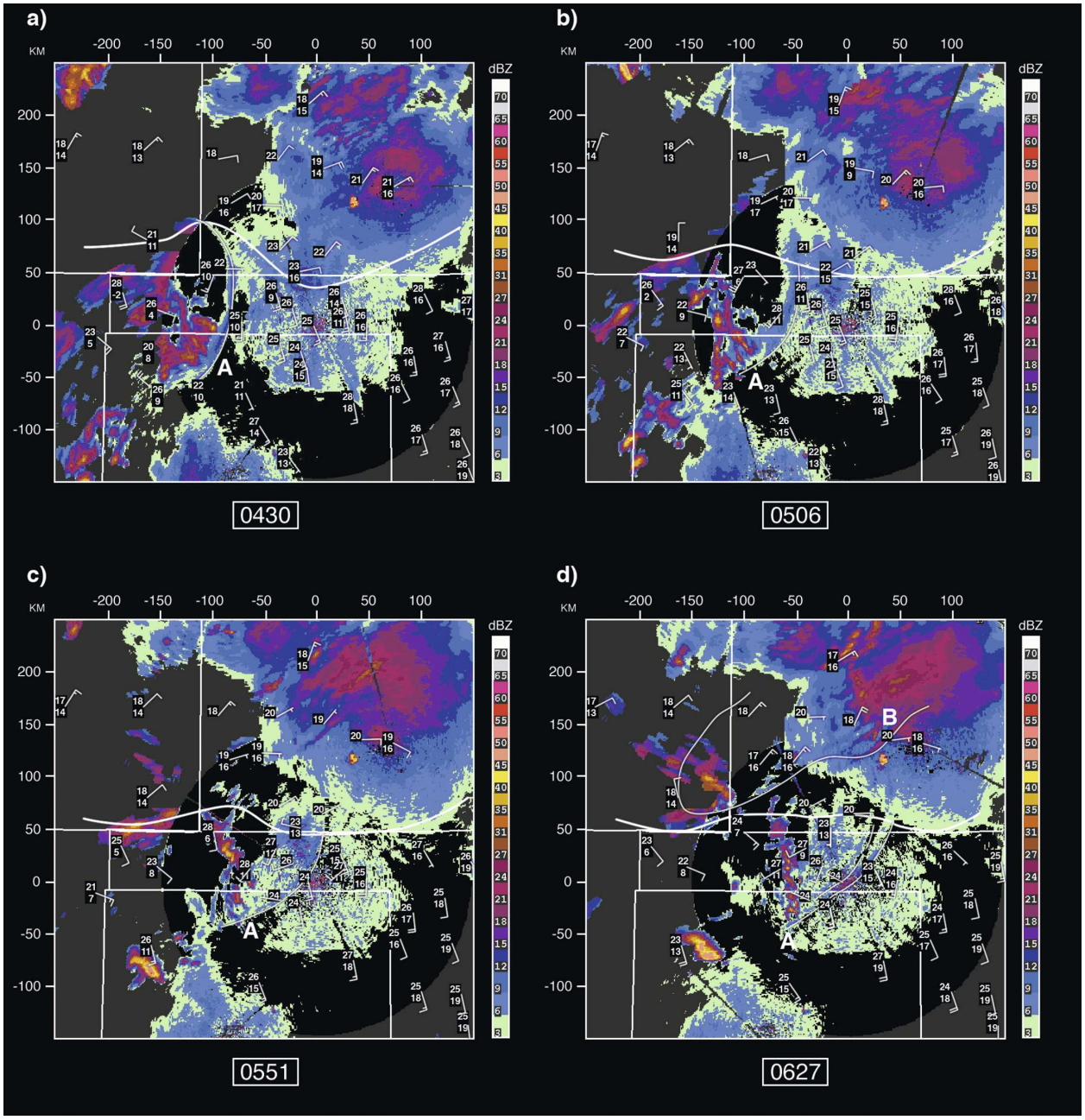

FIG. 2. Multiradar composite reflectivity display (dBZ) and surface mesonetwork plot [temperature and dewpoint (°C) and winds] for (a) 0430, (b) 0506, (c) 0551, and (d) 0627 UTC 4 Jun 2002. Radars used in the composite display consist of the Weather Surveillance Radar-1988 Doppler (WSR-88D) radars in the area plus the S-Pol radar at Homestead (black circular region depicts 150-km range from S-Pol). Thin white line demarcates a convergence boundary originating from storms in the western Oklahoma Panhandle that evolved into the bore/soliton system A by 0430 UTC. Thicker east–west line denotes a quasi-stationary synoptic frontal system. Soliton passes through the Homestead region immediately after 0627 UTC.

results using the Eta Model PBL scheme (Janjić 1994). As the dissimilarity of the results from the control run was quite minor, these results are not shown here.

Dispersion of water vapor and aerosols is enhanced by the interaction of vertical shear and buoyancy. Under stable conditions, vertical mixing is delayed until the Richardson number becomes small enough to permit development of turbulent bursts (Moran 2000). The turbulent kinetic energy (TKE) provides the most direct measure of the turbulence intensity. The prognostic equation for TKE [$\equiv q^2 = \frac{1}{2}(u'^2 + v'^2 + w'^2)$] is (Arya 2000)

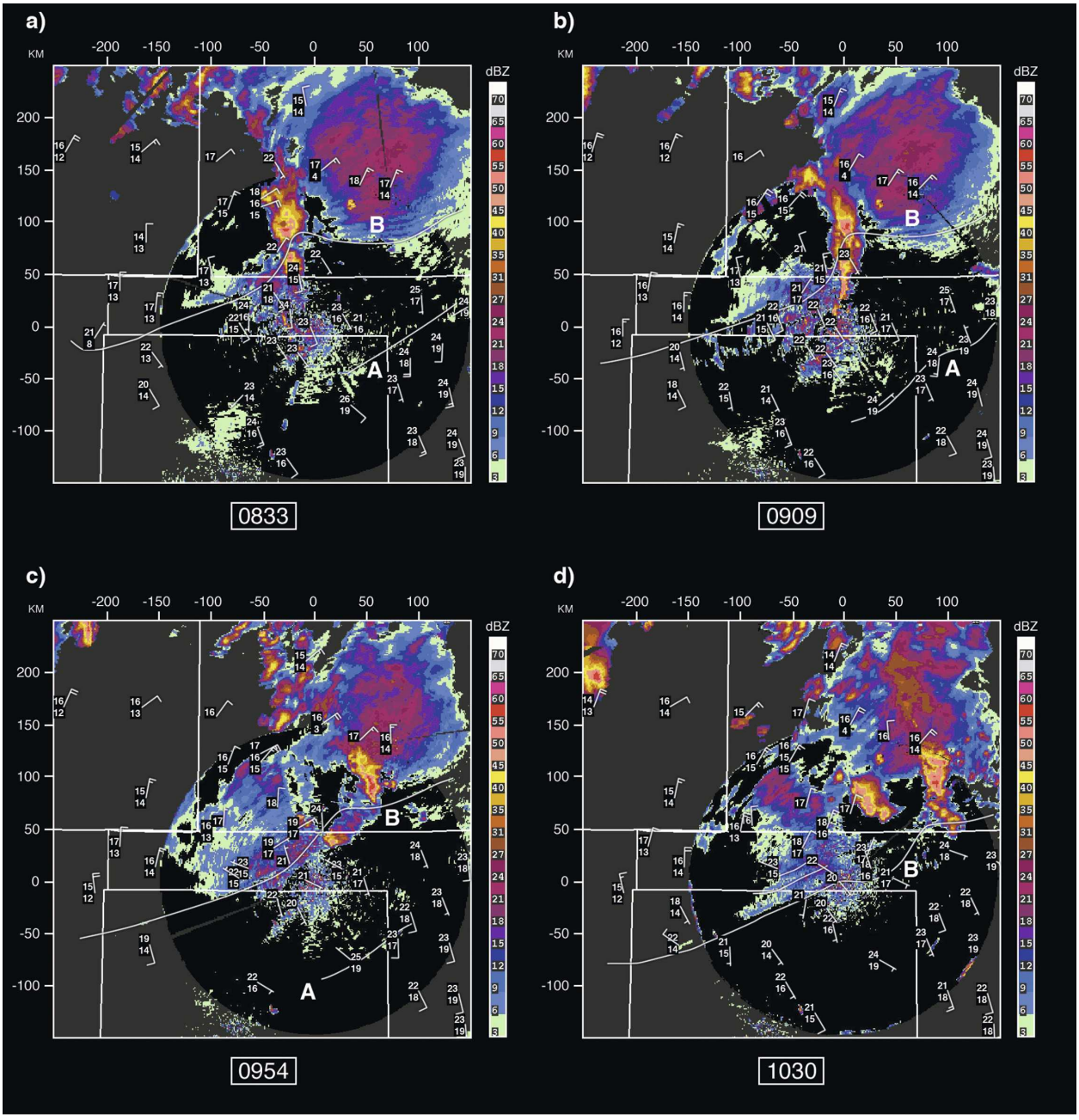

FIG. 3. As in Fig. 2 but for (a) 0833, (b) 0909, (c) 0954, and (d) 1030 UTC 4 Jun 2002. Bore/soliton B originates from a density current that developed to the north of the frontal system in southwestern Kansas in response to convection there.

$$\frac{\partial q^2}{\partial t} = \frac{1}{2}\frac{\partial}{\partial z}\left(\lambda l q \frac{\partial q^2}{\partial z}\right) - \overline{u'w'}\frac{\partial u}{\partial z} - \overline{v'w'}\frac{\partial v}{\partial z} + \frac{g}{\Theta_v}\overline{w'\theta_v'} - \frac{q^3}{\alpha l}, \tag{3}$$

where turbulent fluctuations are denoted by primes. The first term represents the vertical diffusion of TKE; $-\overline{u'w'}\partial u/\partial z$, $-\overline{v'w'}\partial v/\partial z$, and $(g/\Theta_v')\overline{w'\theta_v'}$ are the turbulent fluxes of u momentum, v momentum, and buoyancy; and $-q^3/\alpha l$ is the energy dissipation term (λ is the large-eddy length scale and α is a scaling parameter). At a grid-mesh size of 0.7 km, the MM5 model simulations approach the energy-containing eddy range of resolved turbulence. Although a true large-eddy simulation would require further decrease in the mesh size

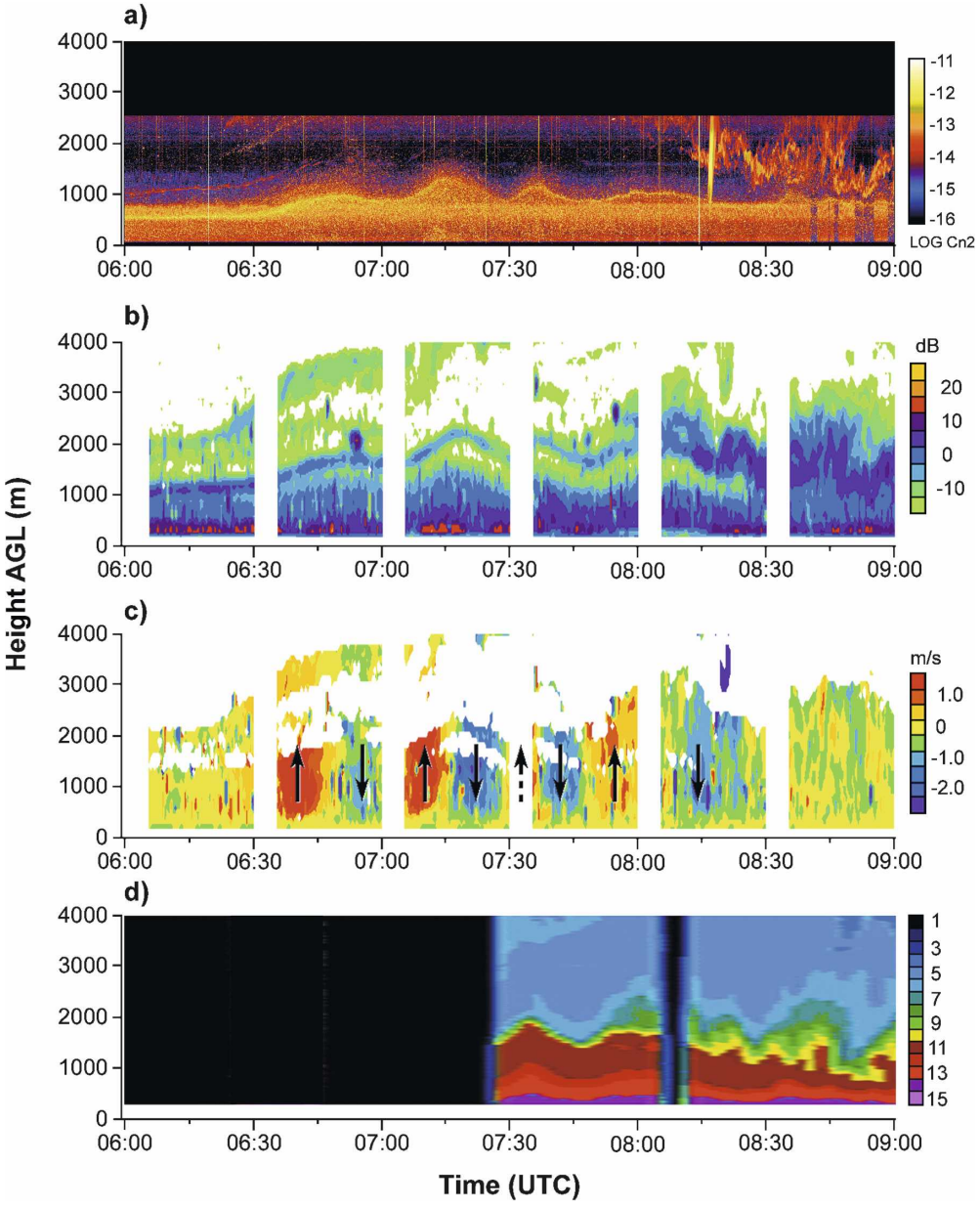

FIG. 4. (a) FM-CW reflectivity (turbulence structure function C_n^2 units), (b) MAPR signal-to-noise ratio (dB), (c) MAPR vertical motions (m s^{-1}; red are updrafts, and blue are downdrafts), and (d) SLR mixing ratios (g kg^{-1}) for the period 0600–0900 UTC. Displays extend to 4.0 km AGL for purpose of making comparisons, though there are no FM-CW data above 2.5 km. Bore A passes sensors at 0630 UTC, resulting in sudden deepening of the stable boundary layer originally of 0.7-km depth to ~1.3-km depth, followed by three amplitude-ordered solitary waves.

by a factor of ~10, an inverse cascade of energy toward larger scales from the resolvable scales may yet occur in the finest-mesh model run (Fedorovich et al. 2004).

4. Observational analyses

Bores are readily identifiable in surface data by a pressure jump to a sustained higher pressure, a shift of the winds into the direction from which the bore is propagating, and a lack of any discernible surface cooling (Smith 1988). The various IHOP remote sensors sampled two bores during the early morning hours of 4 June 2002. Bore A developed from an outflow boundary that originated from convection in eastern New Mexico and crossed the Oklahoma Panhandle to the south of a quasi-stationary synoptic frontal boundary

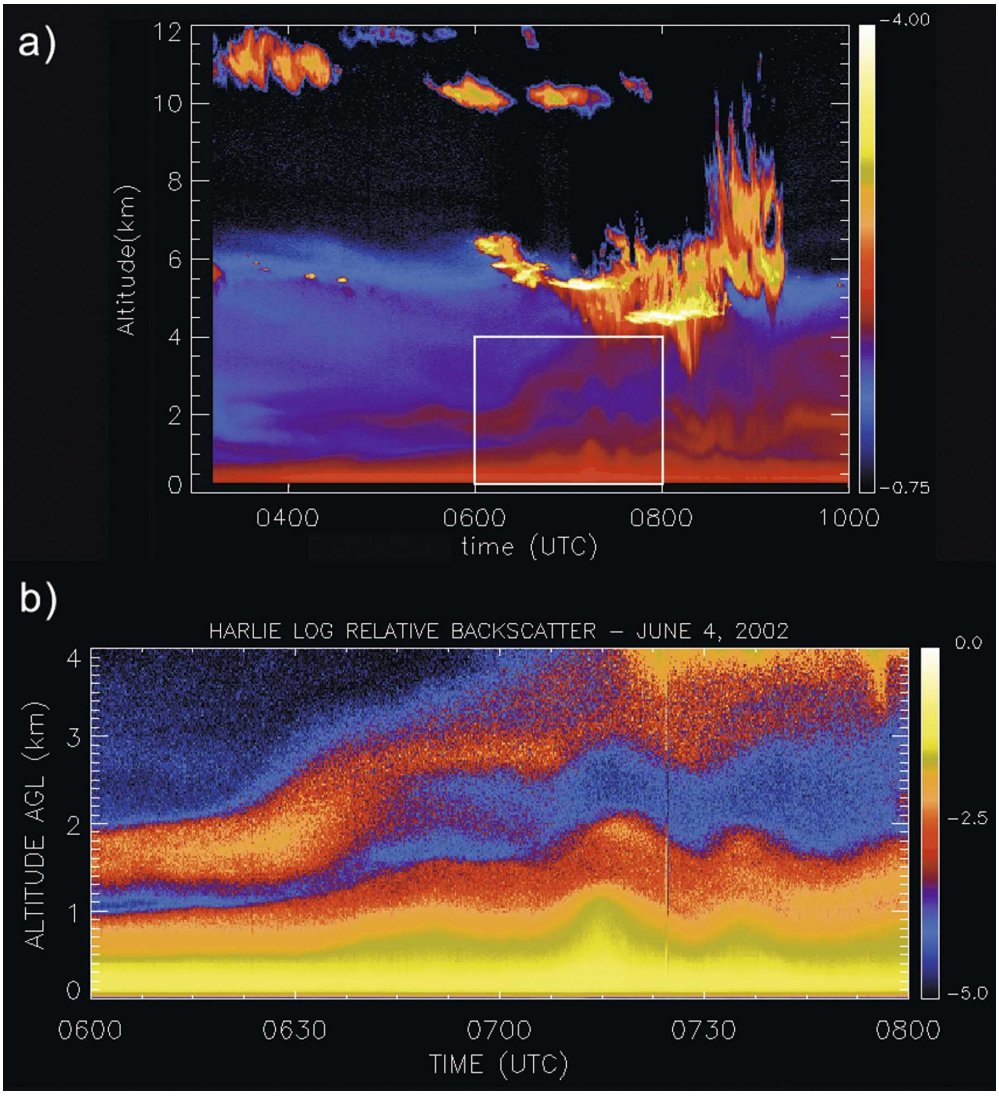

FIG. 5. HARLIE aerosol backscatter logarithmic signal displays of (a) the lowest 12 km of the atmosphere from 0300 to 1000 UTC and (b) the lowest 4 km of the atmosphere from 0600 to 0800 UTC [region depicted by white box in (a)]. The stable boundary layer structure associated with the nocturnal inversion is disrupted by passage of bore A at 0630 UTC. Aerosols are subsequently wafted through a 4-km-deep layer.

(note the stronger northerly winds and cooling to the north of the front in Fig. 2). The temperature contrast across the outflow boundary had already disappeared by 0430 UTC (Fig. 2a), 2 h prior to its passage through the Homestead region (Fig. 2d), yet a distinct clockwise shift in the winds across the boundary persisted over this time. Bore B appears to have developed from a density current arising from postfrontal precipitation in west-central Kansas (Figs. 2d and 3a). As the density current merged with the synoptic frontal boundary, the front began to propagate southeastward, a "fine line" became apparent in the radar imagery (Fig. 3b), and the cooling attending the outflow diminished. This developing bore reached the Homestead network shortly after 1030 UTC (Fig. 3d), by which time there was no discernible cooling associated with its passage. Additional evidence that both of these features were actually bores during their passage through the Homestead network is provided in the following section.

a. FM-CW, MAPR, SRL, and HARLIE observations

Bore A is readily apparent in the FM-CW reflectivity data (Fig. 4a) and the MAPR reflectivity and vertical motions (Figs. 4b,c), but the SRL mixing ratio data (Fig. 4d) were missing around the time of bore passage

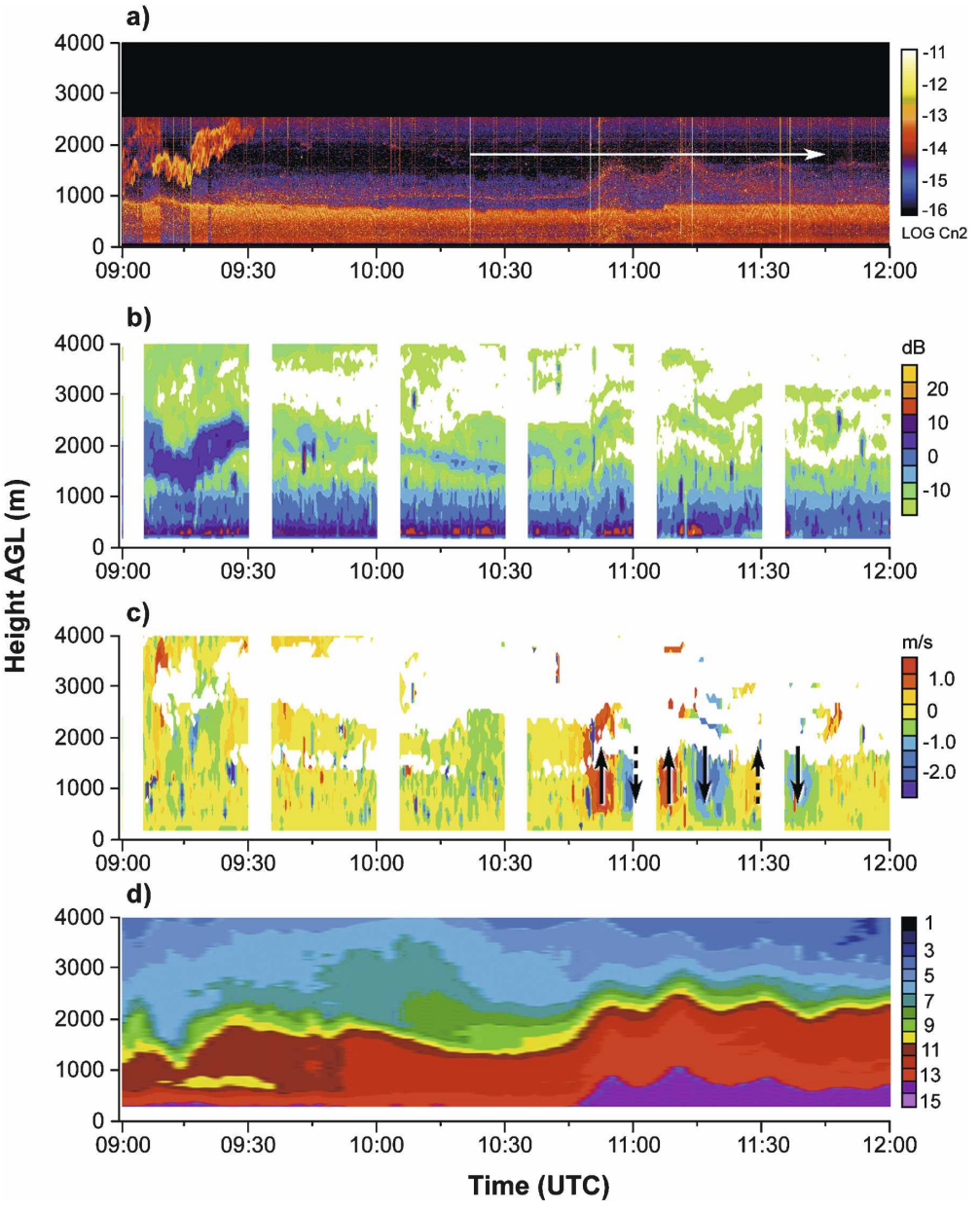

FIG. 6. As in Fig. 4 but the displays cover the period 0900–1200 UTC. Bore B passes at 1050 UTC, resulting in further boundary layer deepening and mixing to 2.3 km in SRL data (less in the FM-CW display, due to signal degradation), but the subsequent wave train lacks the amplitude ordering seen with bore A. White arrow in (a) depicts flight of UW King Air through the solitary wave crests at 1850-m altitude.

(0630 UTC). The bore had already evolved into a soliton composed of waves with a horizontal wavelength of ~15 km.[1] The depth of the antecedent PBL [0.75 km estimated from the sharp vertical gradient in FM-CW signal strength (Fig. 4a)] abruptly jumps to 1.3 km following the passage of the bore front at 0630 UTC. The MAPR signal-to-noise ratio data (Fig. 4b) imply an *indirect* influence of the bore to >3 km (increasing with the passage of the second and third waves at 0705 and 0735 UTC). "Indirect influence" here refers to induced gravity wave motions above the body of fluid contained within the bore (i.e., air originally contained beneath

[1] This wavelength was estimated using time-to-space conversion and the bore propagation speed of 9.8 m s^{-1}, the latter having been measured by the movement of the pressure jumps detected in mesonet time series data as well as the movement of fine lines in S-Pol imagery.

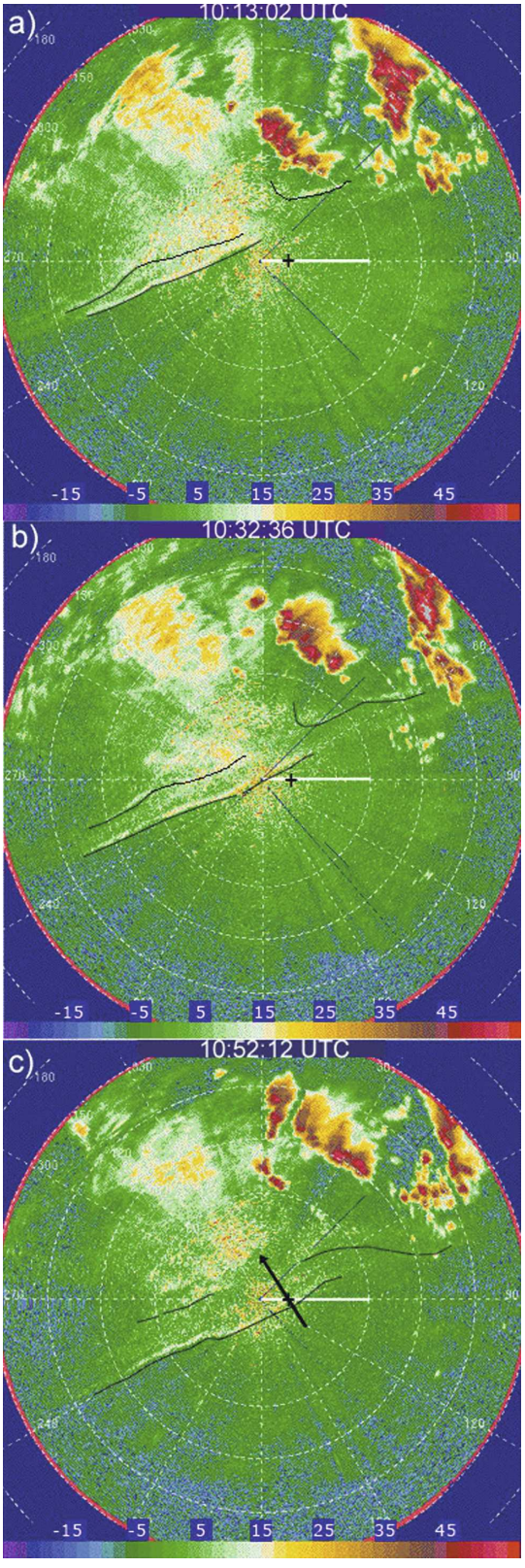

the low-level inversion). The MAPR data reveal a quadrature (90°) phase relation between the vertical motions (Fig. 4c) and fluctuations in the height of the inversion (Fig. 4b). This is characteristic of gravity waves, including solitary waves (Smith 1988; Koch and Clark 1999). Maximum updrafts exceed 2 m s^{-1} below 2 km, but average ~1 m s^{-1} over the 10-min bore lifting periods, resulting in 0.6 km of lifting. This agrees quite well with the observed increase of the PBL depth.

HARLIE observations of aerosol backscatter returns are shown in Fig. 5a for the lowest 12 km of the atmosphere for a ±3.5-h period of time surrounding the passage of bore A and in Fig. 5b for the lowest 4 km for a ±1.0 h time segment centered on 0700 UTC. The larger-scale display illustrates the effects of mixing by the bore and subsequent waves, as aerosols are wafted through a 4-km-deep layer by passage of the soliton; in addition, there is evidence of cloud development well above the bore. The zoomed-in display presents a clear picture of the bore and subsequent waves, and their influence on lifting an elevated layer of high aerosol content originally present in the 1.5–2.0-km layer to above 4 km. This influence is likely the indirect result of lifting above the bore associated with upward propagation of gravity wave energy, which promoted mixing and possible cloud development at higher altitudes.

FM-CW, MAPR, and SRL displays near the time of passage of bore B are presented in Fig. 6. The PBL is less well defined in the MAPR display than seen prior to the passage of bore/soliton A because of the vigorous mixing associated with that bore. In fact, the PBL appears to have developed a dual structure, as shown in Fig. 6b by an elevated inversion that descends in elevation from 2.3 km at 0930 to 1.6 km by 1030 UTC, in addition to a rather unchanging surface-based inversion at a height of 1.1 km.

A quadrature phase relation existing between the MAPR vertical motions associated with bore B and the oscillations of the inversion surface once again supports a solitary wave interpretation. The MAPR vertical velocities, as well as the FM-CW data, suggest the presence of two solitary waves following the bore front. These waves display a horizontal wavelength of ~8 km,

←

FIG. 7. S-Pol radar reflectivity (dBZ) at 0.0 elevation angle at (a) 1013, (b) 1033, and (c) 1052 UTC. White horizontal line shows 60-km scale. Homestead is located at +. Long sinewy line is the bore front. Shorter line to its northwest is a solitary wave, which lags the bore. Curvy line to the northeast is the outflow boundary produced by convective cells. Black arrow in (c) depicts flight track of UW King Air at 1850-m altitude.

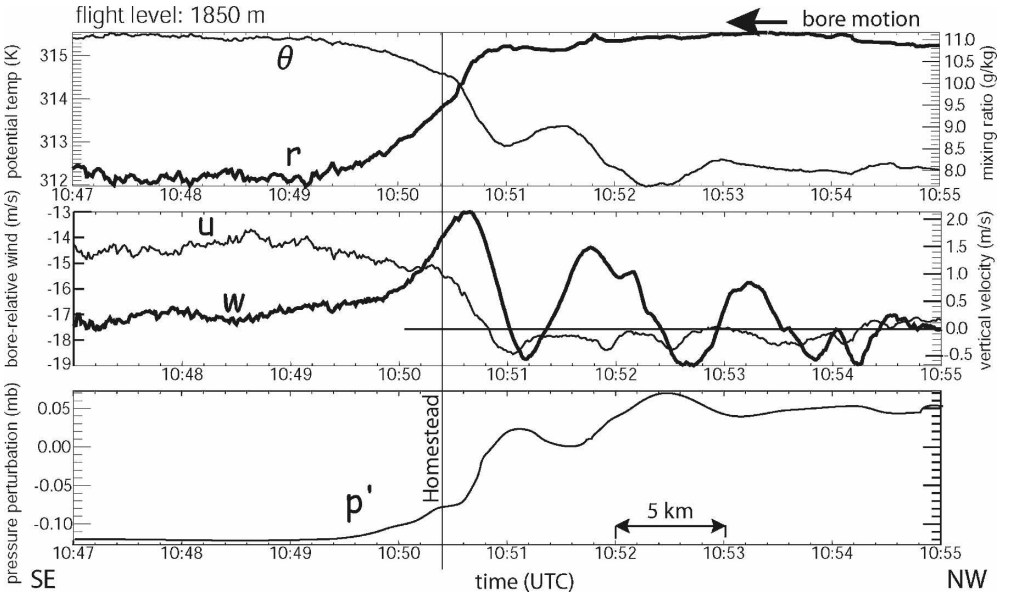

FIG. 8. Flight-level data from UW King Air flight measured from 1047 to 1055 UTC along a track perpendicular to bore B at 1850 m AGL. Shown are traces of (a) potential temperature (K; light line) and mixing ratio (g kg^{-1}; thick line), (b) bore-relative wind component assuming a bore velocity of 10.2 m s^{-1} from 330° (m s^{-1}; light line, with negative values indicating flow from the front to the back of the bore) and vertical velocity (m s^{-1}; thick line), and (c) pressure perturbation (hPa). Flight track is shown in Figs. 6 and 7. Aircraft passed through the bore front at nearly the same time that the bore passed over Homestead (1050:24 UTC).

as estimated using a propagation speed of 6.9 m s^{-1} determined from sequences of S-Pol reflectivity imagery (the trailing line to the northwest of the bore front in Fig. 7). Since the speed of bore propagation was 10.2 m s^{-1}, the implication is that the solitary waves lagged the bore. A unique property of solitary waves is that the speed of wave propagation is proportional to their amplitude. The relative difference in speed between the bore front (the leading wave with largest amplitude) and the waves of smaller amplitude that followed the bore reflects this fact.

b. *UW King Air observations*

Solitary waves associated with bore B also are readily apparent in data collected in situ by the UWKA aircraft as it flew a number of sorties near Homestead perpendicular to the bore front. The flight leg at the 1850-m altitude (Fig. 7c) was the only one that intercepted the bore front and the crests of the solitary waves (Fig. 6a). The data measured during this flight from 1047 to 1055 UTC (Fig. 8) show that the aircraft intercepted the bore at 1050:25 UTC just as it was passing over the Homestead facilities. Also apparent are two amplitude-ordered solitary waves with horizontal wavelengths of ~7 km. Considering the UWKA, FM-CW, and MAPR data together, we conclude that the average horizontal wavelength of the solitary waves was 8.3 ± 1.3 km. The antiphase relationships seen between perturbations in potential temperature and pressure, and quadrature (quarter-wavelength) relationships between potential temperature and vertical velocity perturbations, are both characteristics of solitary waves.

Changes experienced by the UWKA as it penetrated the bore consisted of 3 g kg^{-1} moistening, 3°C cooling, and 4 m s^{-1} increase in wind speed directed toward the rear of the bore. The sustained nature of the changes supports the interpretation of their source being a bore. The small 0.15-hPa magnitude of the pressure jump suggests that the bore was not much deeper than the flight level. Assuming that the temperature perturbation and the base-state potential temperatures are independent of height, then Eq. (2) predicts that the top of the bore was 2.2 km, or only 0.3 km above the flight level. This bore depth from the UWKA data is comparable to the ~2.0 km estimate from FM-CW and the ~2.7 km obtained from MAPR (though it is difficult to separate the bore top from layers of atmosphere lifted above the bore in the MAPR display). We suggest that a best estimate of the bore depth is 2.3 ± 0.3 km.

c. *AERI observations and the role of the bores in convective initiation*

AERI data provided unique insight into the thermodynamic structures associated with the bores. Time–

height displays of potential temperature, relative humidity, and mixing ratio in the lowest 2.5 km of the atmosphere (Fig. 9) clearly reveal the passage of both bores. The bore signature consists of an abrupt cooling of 1°–3°C (strongest in the 500–1200-m layer) and rapid moistening throughout this layer. The lack of near-surface cooling is characteristic of bores (Smith 1988; Koch and Clark 1999). A rapid increase of mixing ratio occurs with bore A, but less so with bore B, primarily because ample moisture had been diffused throughout a 2-km-deep layer by the earlier passage of bore A and the subsequent wave train (resulting in a *doubling* of the precipitable water from the surface to 2.5 km).

Thermodynamic soundings derived from the AERI data at approximately 2-h intervals and the two Homestead ISS soundings from 0401 and 1045 UTC are shown in Fig. 10. The variations in convective available potential energy (CAPE), convective inhibition (CIN), and the lifting condensation level (LCL) shown on these individual sounding plots primarily reflect lower-tropospheric changes detected in the AERI measurements. Prior to the passage of bore A, a strong inversion was present—at 835 hPa at 0401 UTC (Fig. 10e) and at 800 hPa at 0602 UTC (Fig. 10a). This inversion separated a relatively moist PBL from much drier air aloft and also prevented parcels of air from reaching their level of free convection as indicated by the large CIN value of -970 J kg^{-1} at 0602 UTC. Following passage of bore A, this inversion was weakened considerably and lifted (Fig. 10b); also, substantial moistening of the atmosphere occurred below 700 hPa prior to the appearance of bore B (Fig. 10c). The net effect of the passage of both bores (Fig. 11) was to increase the CAPE modestly, but to reduce the CIN by more than half and decrease the LCL from 740 to 820 hPa. These changes were not quite sufficient to trigger development of deep convection. However, similar destabilization and moistening effects produced locally by bores noted in other studies have sometimes led to triggering of severe convection (e.g., Koch and Clark 1999).

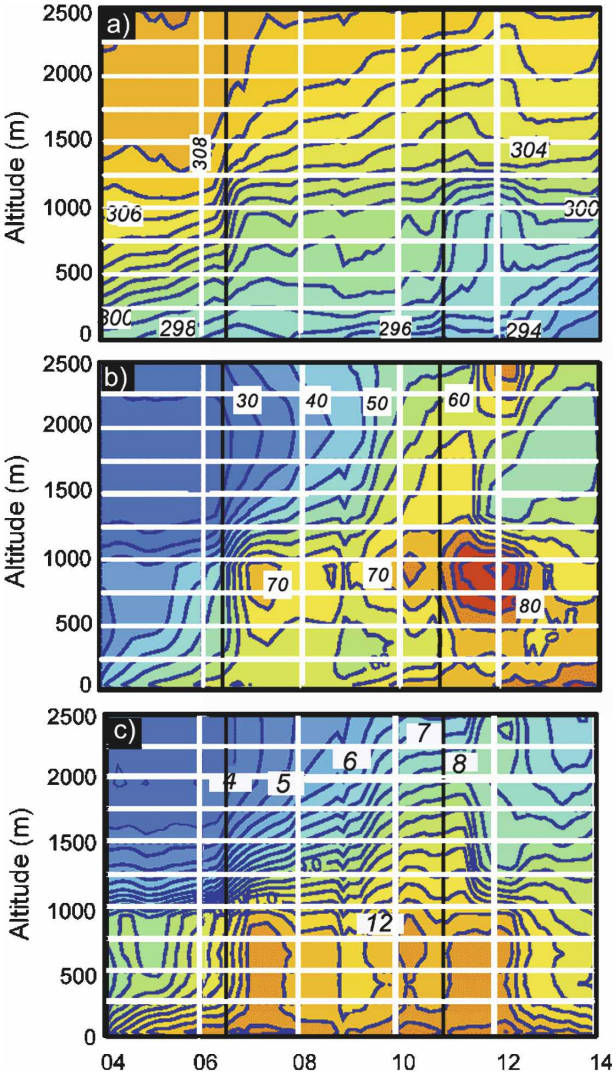

FIG. 9. Time (UTC) vs height (m AGL) displays of thermodynamic properties obtained from AERI measurements: (a) potential temperature (K), (b) relative humidity (%), and (c) mixing ratio (g kg^{-1}). Times of passage of bores A and B are shown with black vertical lines. Short periods of missing data have been interpolated across in this display (but not in Fig. 18, which uses the full high-resolution data).

d. *Mesoscale surface analyses*

The collection of surface mesonets in IHOP made it possible to track the evolution of surface convergence boundaries. This task was much simpler for stations that had 1–5-min observations; however the paucity of such data in the western Oklahoma and Texas Panhandles (Fig. 1) did present problems. Time series of temperature, pressure perturbation (a simple difference from the value at the time of bore passage), and computed refractivity changes from stations VERL and HISS are shown in Fig. 12. Passage of bore A at VERL was marked by a 1.9-hPa pressure jump at 0520 UTC and by a less abrupt 1.3-hPa increase at HISS at 0628 UTC, which is indicative of the weakening of the bore as it progressed toward the HISS remote sensing facility. Two amplitude-ordered solitary waves are evident in the VERL trace. More waves are detectable at HISS, but they lack the amplitude ordering seen earlier. Insignificant cooling occurred with the bore at both stations. Slight warming accompanied the passage of the first solitary wave. Refractivity changes are dramatic at VERL (a decrease exceeding 10 N units during the pressure jump), as a result of substantial drying at the surface, but are virtually nonexistent at HISS.

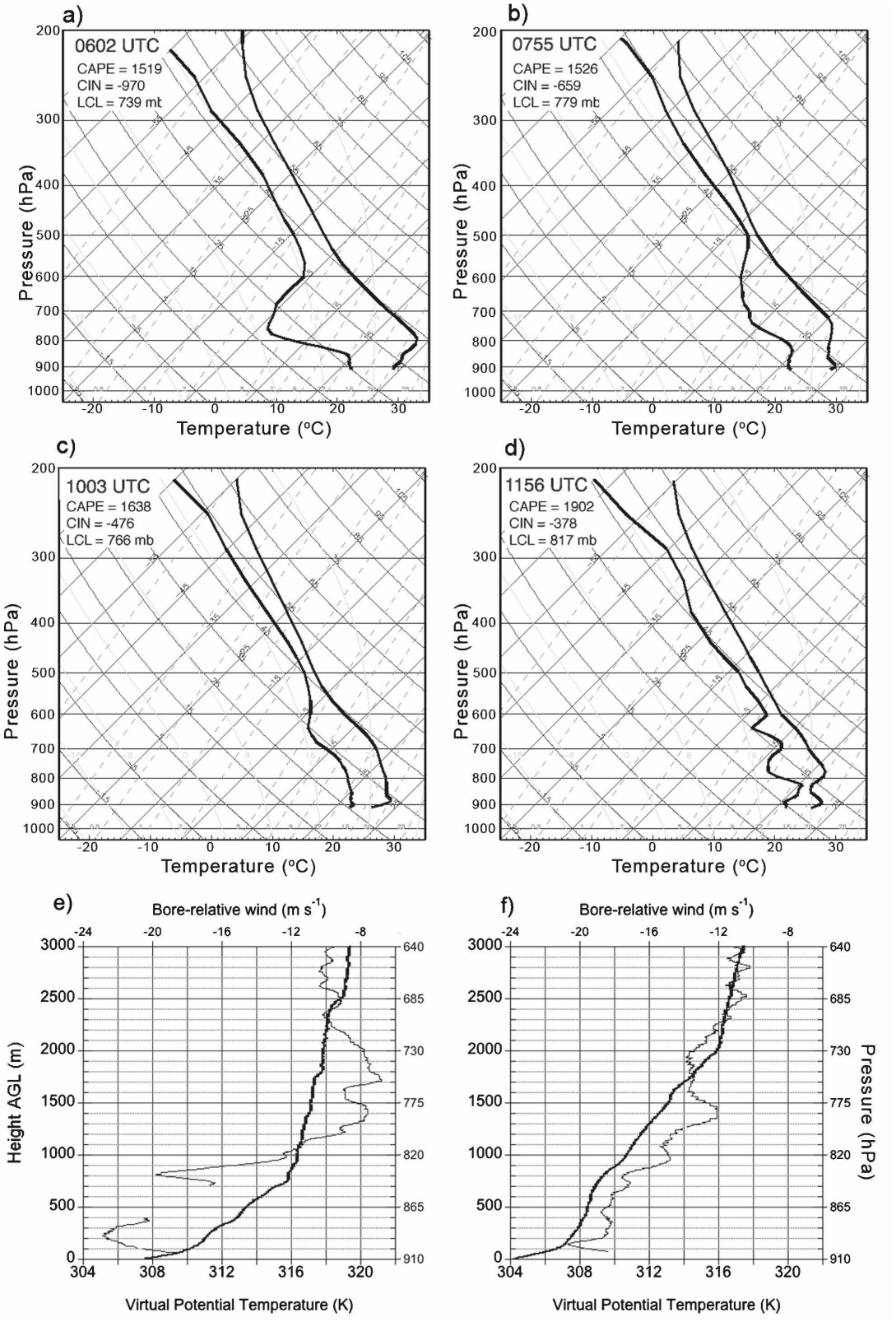

FIG. 10. Skew T–log$p$ thermodynamic charts derived from AERI measurements at approximately 2-h intervals: (a) 0602, (b) 0755, (c) 1003, and (d) 1156 UTC, and profiles of virtual potential temperature (K; dark lines) and bore-relative winds (m s^{-1}; light lines) from Homestead ISS soundings at (e) 0401 and (f) 1045 UTC. Since AERI measurements are gradually blended with analyses from the RUC model above 2.5 km, soundings above 700 hPa do not represent the AERI data.

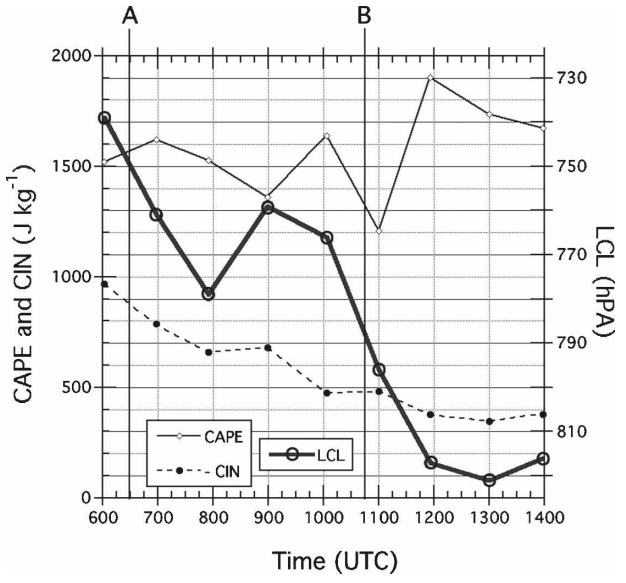

FIG. 11. Temporal variations in the CAPE (J kg^{-1}), CIN (J kg^{-1}), and LCL (hPa) from AERI soundings at the times shown by the markers (approximately hourly).

The changes accompanying passage of bore B at RUST and HISS are shown in Fig. 13. Bore B produced a 1.3-hPa pressure rise at RUST at 1036 UTC and a 1.8-hPa rise at HISS at 1042 UTC, but with 1°C cooling at RUST and 1.4°C warming at HISS. Note that neither temperature change is sustained, in contrast to the pressure changes, further evidence that both phenomena are bores. Refractivity changes were pronounced at RUST (a sudden increase of 3 *N* units followed immediately by a large decrease of 6 *N* units)—the result of moistening followed by drying—but are negligible at HISS.

By plotting such changes at all mesonet stations on maps, spatial interrelationships become apparent (Figs. 14 and 15), allowing for clear identification of the evolution of the density currents into bores. The isochrones of the times of passage of the pressure jump lines were used, in conjunction with the S-Pol fine line analyses, to determine the propagation velocities for the density currents and bores. The pressure jumps were consistently strongest during the early stages when cooling occurred with the jumps, indicating the presence of a

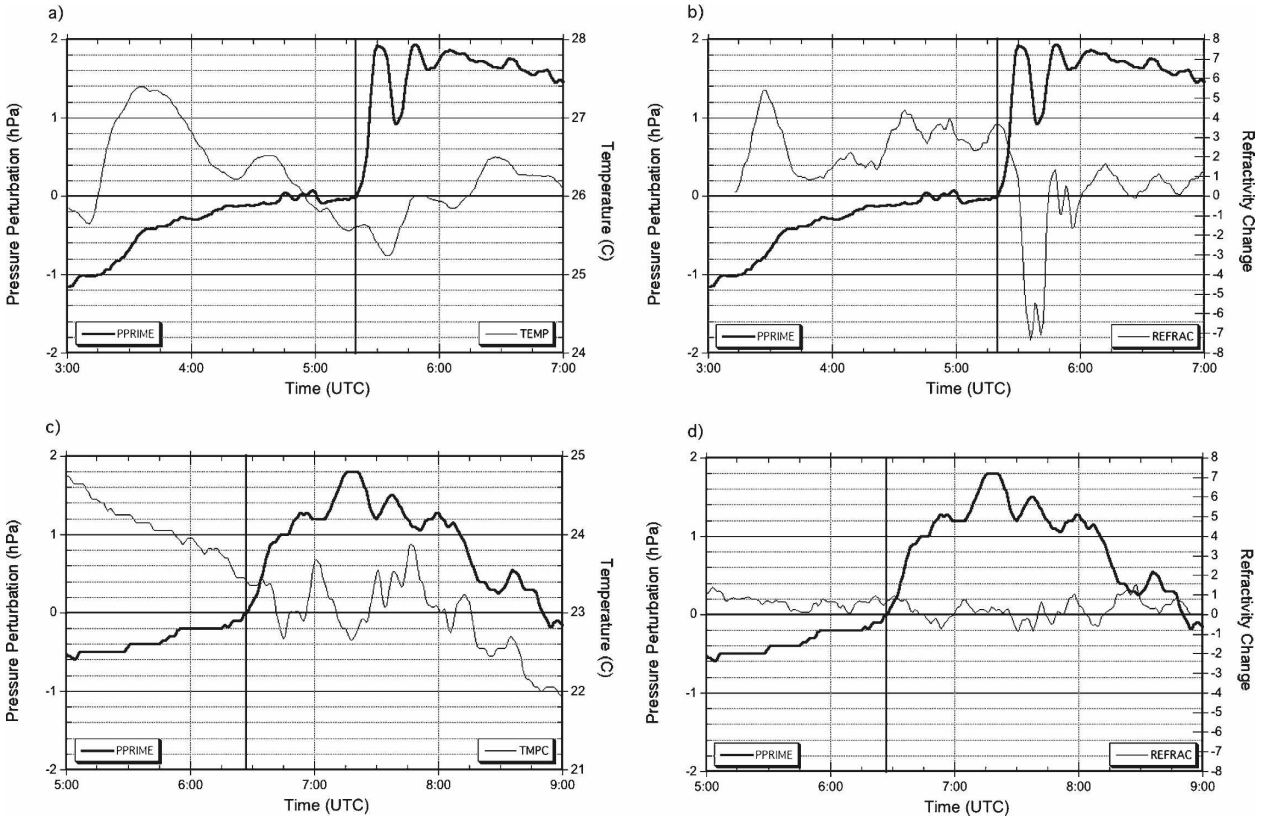

FIG. 12. Time series of (a) temperature (thin lines; °C) and pressure perturbation (thick lines; hPa) from station VERL (Fig. 1), (b) refractivity change (thin lines; *N* units) and pressure perturbation (thick lines; hPa) from VERL, (c) temperature and pressure perturbation from station HISS, and (d) refractivity change and pressure perturbation from station HISS. Bore A passes through VERL and HISS at 0520 and 0630 UTC, respectively.

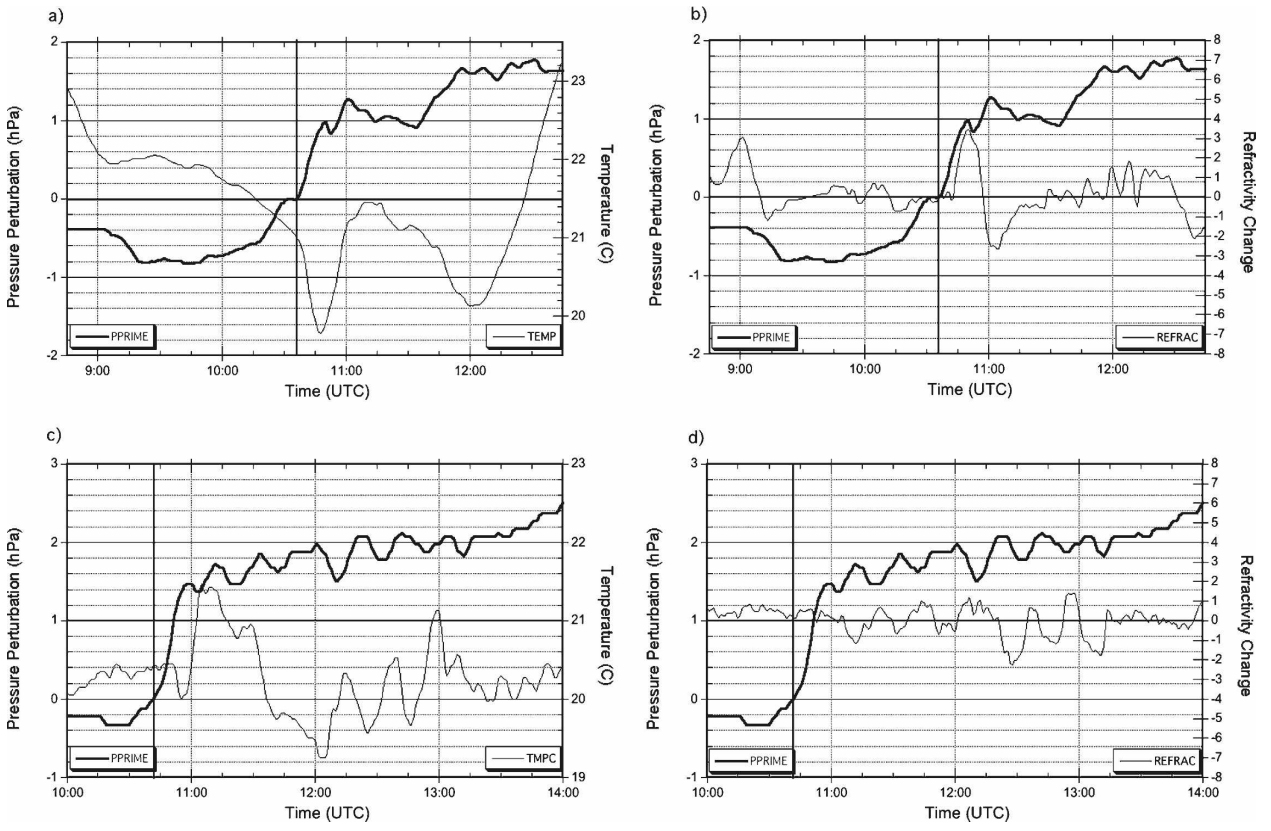

FIG. 13. As in Fig. 12 but for time series from stations (a), (b) RUST and (c), (d) HISS for bore B. Bore B passes through RUST and HISS at 1036 and 1044 UTC, respectively. Cooling and strong refractivity changes accompany bore B at RUST at this time, when the ground-based remote sensing systems detected the passage of the bore. These signatures are not present at HISS, even though the two events are only minutes apart.

density current structure at those times. The cooling associated with density current B was much stronger than that detected with system A and also had two points of origin—one over extreme southwestern Kansas and a second one over southern Kansas to the north of Homestead (Fig. 15c). The density currents evolved into bores as the cooling signature was replaced by warming. This occurred quickly for bore A (Fig. 14) but, because of the stronger initial cooling with density current B and the reinforcement of cooling in the central Oklahoma Panhandle, the warming associated with bore B was delayed and weaker. The following sequence of events characterized both bores: first, the strong pressure jump associated with the cooling, followed by maximum surface warming downstream of the pressure jump region, and finally, the strongest refractivity (thus, moisture) decreases. The probable cause for this curious behavior is discussed immediately below.

e. Refractivity changes

Near-surface refractivity (N) change fields computed from S-Pol and surface mesonet data during the times of bore passage are displayed with mesonet temperature and wind observations in Fig. 16. The radar-derived band of pronounced rate of decrease in N (-7 units in 12 min) occurring in association with the passage of bore A in the central Oklahoma Panhandle region (Fig. 16a) is comparable to the -10 N changes at VERL. The mesonet data showed that the primary cause for this sudden decrease in refractivity was a rapid drop in water vapor mixing ratio [the moist term in Eq. (1)]. However, this band virtually disappeared during its short progression to the Homestead facility (Fig. 16b), in excellent agreement with the mesonet refractivity changes shown. Refractivity changes accompanying the passage of bore B were weaker and less organized compared to bore A (Fig. 16c) and, once again, the band of refractivity decrease nearly disappeared by the time it reached HISS (Fig. 16d).

The refractivity changes computed from S-Pol and the surface mesonet traces were in good agreement overall, as the correlation coefficient was 0.88 (Fig. 17a). The temperature and mixing ratio data collected by AERI were also used to estimate refractivity

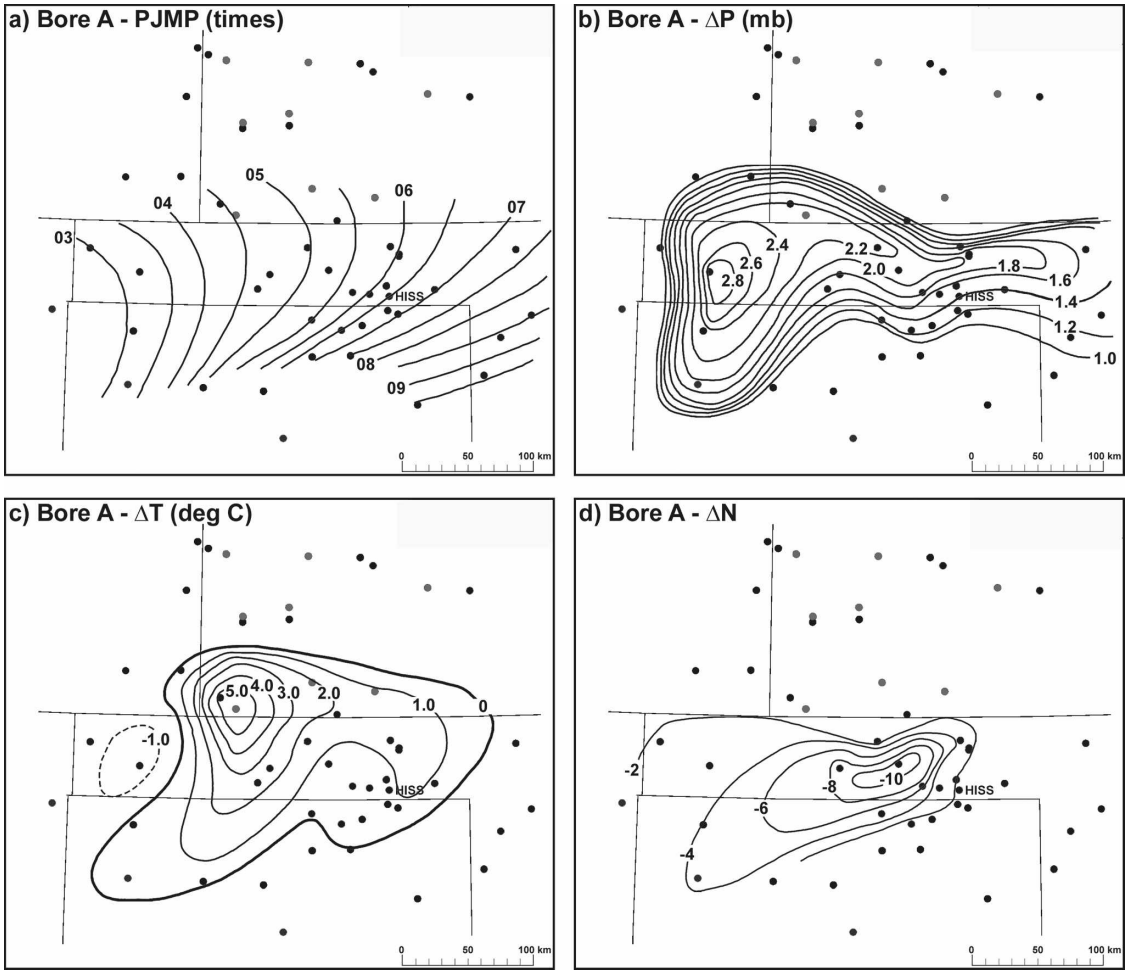

FIG. 14. Surface analyses for bore A of (a) isochrones of times of passage of bore pressure jump (30-min UTC intervals), (b) amplitude of pressure jump (0.2-hPa intervals), (c) temperature change associated with bore passage (1.0°C intervals, with cooling denoted by dashed lines), and (d) computed refractivity changes associated with bore passage (2 *N* unit intervals).

changes, and these were compared to estimates from the SRL (though not totally independent, since we applied AERI temperature measurements to the SRL data). This comparison shows that AERI and SRL estimates of refractivity change fluctuations averaged over the 300–500-m layer were also in close agreement (Fig. 17b).

Since the various instrument estimates of refractivity changes have been shown to agree well with one another, these data were examined to understand why the pronounced refractivity decreases near the surface seen only 15 km west of the Homestead facility vanished so quickly. AERI time–height displays over the lowest 2000 m of the atmosphere of refractivity, mixing ratio, and potential temperature, as well as "perturbation" fields (defined as a difference from the average at each level calculated over the entire time window), are presented in Fig. 18. Both bores produced pronounced *increases* of refractivity of ~6–8 units associated with sudden increases of mixing ratio of ~1–2 g kg^{-1} and slight cooling (except for the lowest 50 m). Note also the existence of a very shallow (<200 m deep) moist layer near the surface with no evidence of drying or refractivity decreases. These measurements made by AERI at the Homestead facility and the earlier discussion on refractivity changes computed from S-Pol and the mesonet together suggest that at earlier times, when the bore/soliton system was much stronger, downward mixing of warm, dry air from above the inversion produced substantial surface drying and decreases in refractivity. However, with the demise of the bore/soliton system near Homestead, this mixing became much less vigorous. Consequently, lifting of air by the bore head only produced adiabatic cooling aloft with no surface drying

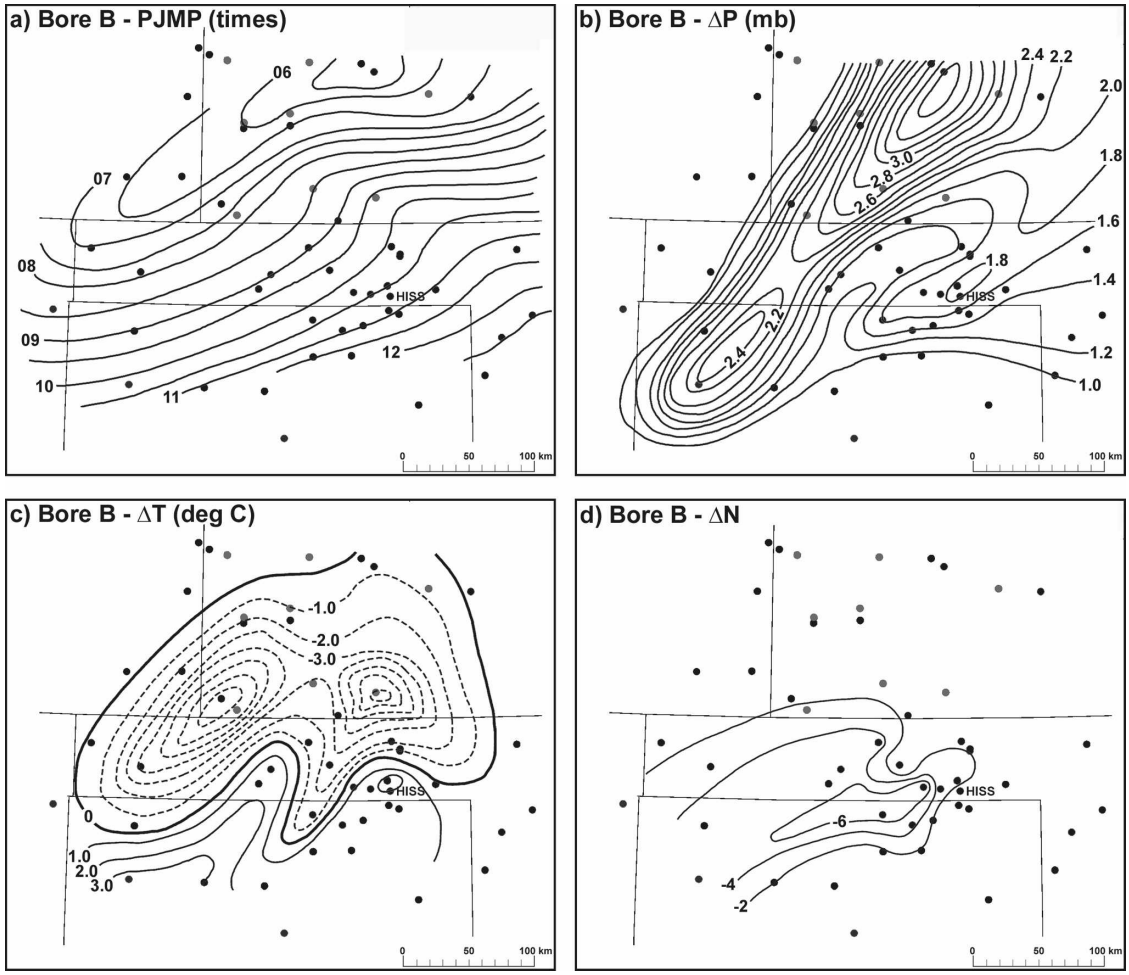

FIG. 15. As in Fig. 14 but for bore B. Strong cooling occurs from the thunderstorm outflow density current prior to bore formation. Indication of a secondary surge of cooling over the central Oklahoma Panhandle in the 0930–1030 UTC time period is associated with the weak outflow boundary discussed earlier (cf. Fig. 7).

and distributed the very moist air near the surface upward through the bore depth and beyond by the waves. This hypothesis lends itself to testing using the numerical model, as discussed next.

5. Numerical model results

The model simulations were unable to reproduce features resembling bore A. The reason for this failure is that the MM5 did not predict any deep convection over New Mexico or the western Oklahoma Panhandle from 0000 to 0900 UTC. On the other hand, the models successfully produced a bore corresponding well in timing and location with observed bore B because they accurately simulated the quasi-stationary frontal system and the postfrontal precipitation. Furthermore, the highest-resolution model was able to produce a soliton from this bore with characteristics (number of waves, horizontal wavelength, amplitude ordering) nearly identical to those observed. These results indicate that the ability of NWP models to simulate observed bores and solitons is predicated on their ability to accurately simulate precipitation and to have sufficient resolution.

a. Sensitivity to model grid resolution

Surface wind divergence and temperature fields predicted by the 2- and 0.7-km model runs are shown in Fig. 19 at two times. The considerable detail present in the divergence fields originates primarily from topographic features, such as over eastern New Mexico, or the pronounced northwest–southeast stationary band in southwestern Kansas associated with the Cimarron River valley (Figs. 19c,d). However, animation of these hourly fields shows a single band that propagates southeastward in a coherent fashion—the strong southwest–northeast band of coupled convergence and divergence

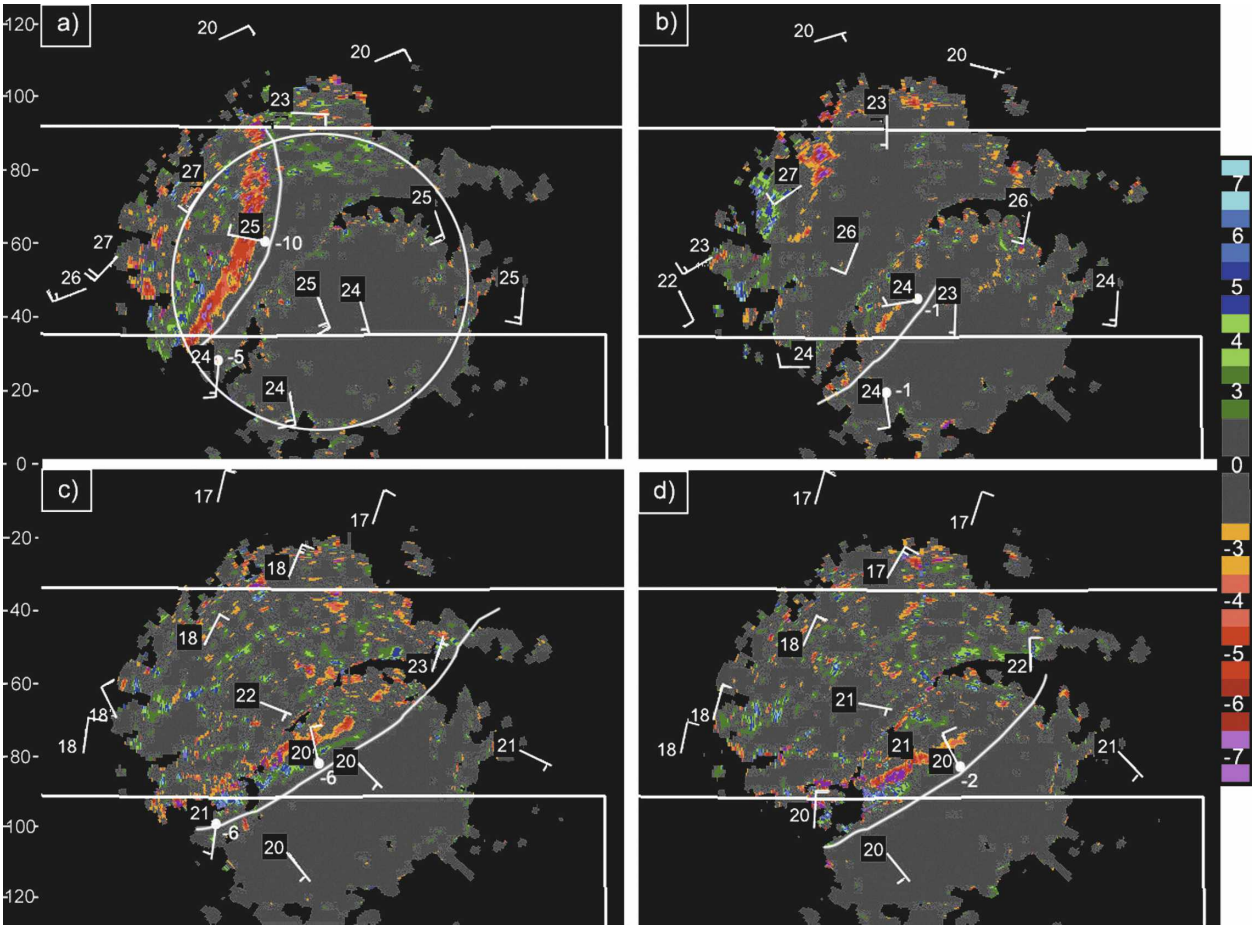

FIG. 16. Refractivity 12-min change fields over the central Oklahoma Panhandle derived from S-Pol measurements for bore A at (a) 0532 and (b) 0632 UTC and bore B at (c) 1032 and (d) 1042 UTC. Radar-derived refractivity changes are in *N* units (color scale on the right). Selected mesonet computed refractivity values are shown during times of bore passage (solid white dots). White curves depict bore location where a radar refractivity signal is apparent. Also shown are local mesonet observations of winds (kt) and temperature by white lettering inside black boxes (°C). Scale on left side of the figure shows distance (km). The 40-km radius range circle from the S-Pol radar is shown in (a). Homestead is 15 km due east of the radar.

extending from the northwestern part of the Oklahoma Panhandle to central Kansas. This band owes its existence to the surface cold front, but the temperature gradient across this band was sharpened by cold pools originating from model precipitation in eastern Colorado to the north of the front. This band is located at the leading edge of the weak frontal zone identifiable in the isotherm packing at 0800 UTC, but 1 h later the band has propagated ahead of this thermal feature. The change in relative position of these features represents the model's transformation from a density current to a bore. The numerically predicted bore passes through Homestead at 1115 UTC, only ~30 min later than observed.

The high-resolution nested grid simulation has the same divergence–convergence band associated with the density current and the bore, but it also contains several parallel bands in the wake of the bore front. These latter features are solitary waves, which are better revealed in a vertical cross section taken perpendicular to the band (Fig. 20d). The solitary waves display amplitude ordering and a horizontal wavelength of 9.3 km, which compares favorably to the 8.3 km averaged from the FM-CW, MAPR, and UWKA data. By contrast, the very weak waves in the 2-km simulation have an average wavelength of 11.6 km. This is smaller than 6 times the grid spacing, so those waves are poorly resolved.

The bore is also clearly present in the coarse and fine grid model forecasts. The antecedent inversion surface is abruptly lifted during the progression of the bore to the southeast at a speed of 8.4 m s^{-1} in the fine-grid simulation (as compared with 10.2 m s^{-1} in the observations and 9.5 m s^{-1} in the 2-km simulation). The parent density current (the cold front) is visible 10 km to

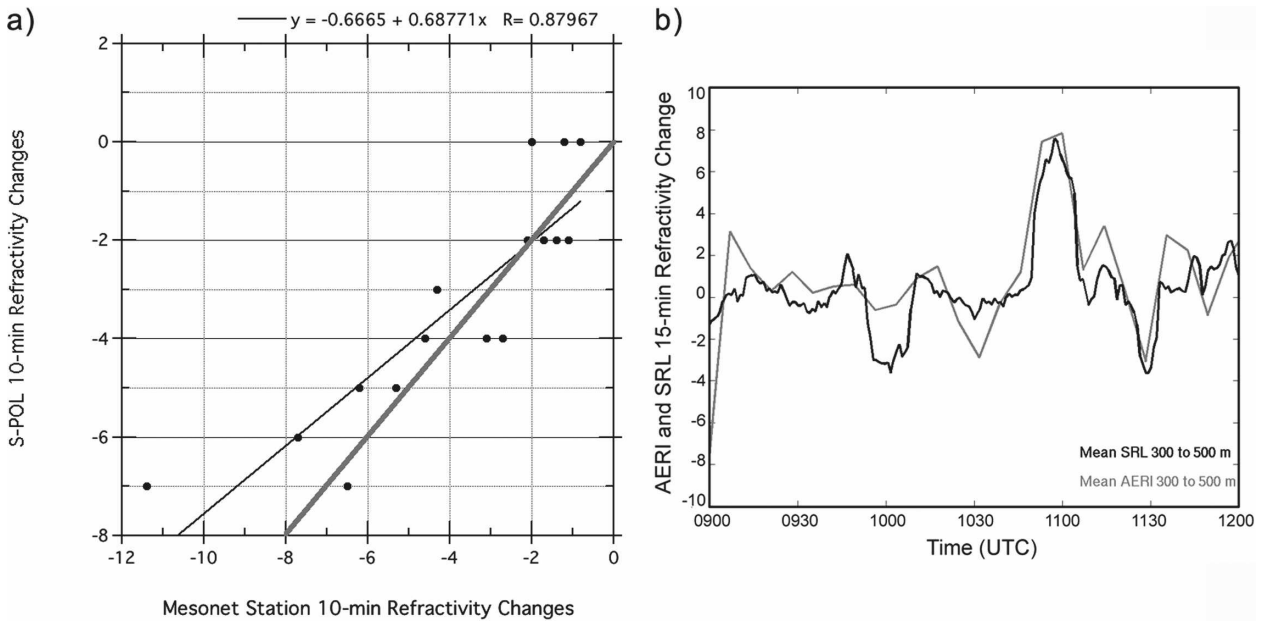

FIG. 17. Comparisons of low-level refractivity changes measured by various observing systems: (a) 10-min refractivity changes derived from S-Pol 0° scan data vs surface mesonet stations, and (b) 15-min refractivity changes estimated from AERI (thin gray line) vs SRL (thick black line) over the 300–500-m layer nearest the surface. Black and thick gray lines in (a) depict line of regression through the data (correlation coefficient $r = 0.88$) and line of perfect correlation, respectively.

the northwest of the incipient bore at 0800 UTC, but this distance increases to nearly 30 km by 0900 UTC as the bore propagates ahead of the density current.

b. Turbulence and mixing in the simulations

The three waves constituting the soliton at 0900 UTC in the fine-grid simulation grew to five waves within one hour (Fig. 21), but did not increase in number afterward. The fine-grid simulation predicts that the intensity of mixing (TKE) is strongest within the moist PBL ahead of the bore, directly behind the bore head, and underneath the solitary waves. The first of these three regions is easily understood to be the result of the shear stress related to the strong along-bore flow associated with the low-level jet [the third term on the rhs of (3)]. This conjecture is supported by an independent calculation of this term (not shown). The other two regions are actually related to the same process, as revealed by the 15-min resolution plots shown in the right half of Fig. 21. A TKE feature highlighted by the arrow in this figure illustrates this process. This local maximum in TKE originates at 0900 UTC just behind the bore head. It is then advected rearward and downward by the vertical motions associated with this wave into the ridge region of the second wave by 0915, where it undergoes vertical deformation. This TKE patch subsequently undergoes a similar process as it progresses through the trough following the second wave and is mixed into the ridge of the third wave. As this feature makes its way rearward and downward, it is increasingly subjected to less static stability and the buoyancy term in (3) becomes more important.

The fine-grid simulation of mixing processes is further understood with the analyses presented in Fig. 22. Two major points can be made. First, mixing ratio is substantially reduced within each solitary wave trough due to entrainment of dry air above the inversion and subsidence (Fig. 22a). These dry intrusions penetrate to within 800 m of the surface. In addition, a drying effect also displaying a wavelike behavior is evident very near to the surface and under the wave train. Between these two regions, a layer of high mixing ratio in excess of 14 g kg^{-1} (also of relative humidity exceeding 90%; not shown) is found. Second, the bore-relative circulation (Fig. 22b) shows the existence of nearly closed circulations beneath each of the waves within 500 m of the surface. Since moisture could not be advected from the rear toward the bore front, any dry air that was brought down to these very low levels by the wave-induced subsidence would be trapped near the surface. In fact, a time–height cross section of mixing ratio variations at the point where the bore front intersects the cross section at 0900 UTC (Fig. 22c) shows the existence of very shallow drying at and following the bore passage. The shallow drying is strikingly apparent in the time series

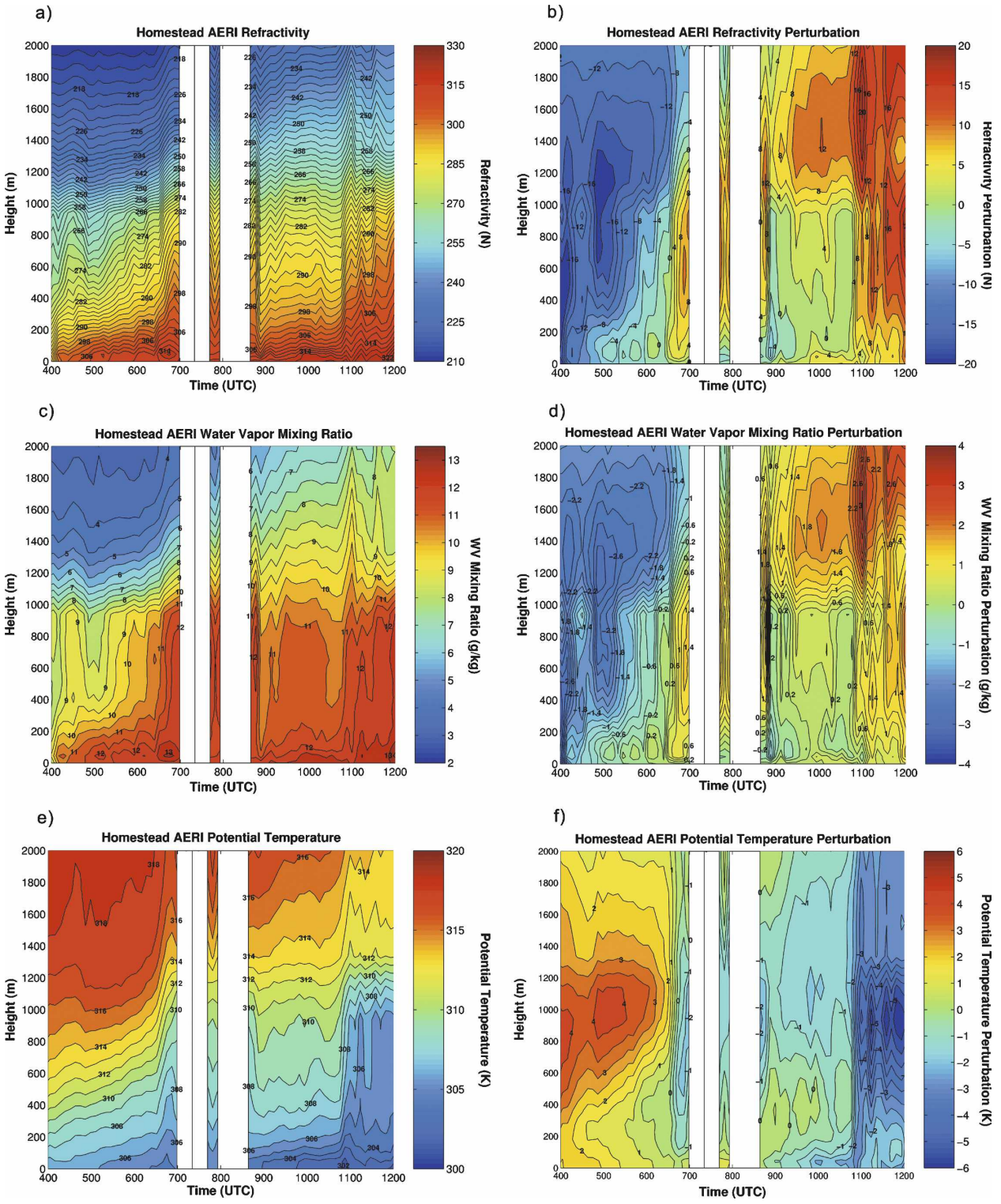

FIG. 18. AERI time–height displays from 0400 to 1200 UTC of (a) refractivity (N units), (b) perturbation refractivity (N units), (c) mixing ratio (g kg^{-1}), (d) perturbation mixing ratio (g kg^{-1}), (e) potential temperature (K), and (f) perturbation potential temperature (K). Passage of bores A and B occurs at 0625 and 1050 UTC.

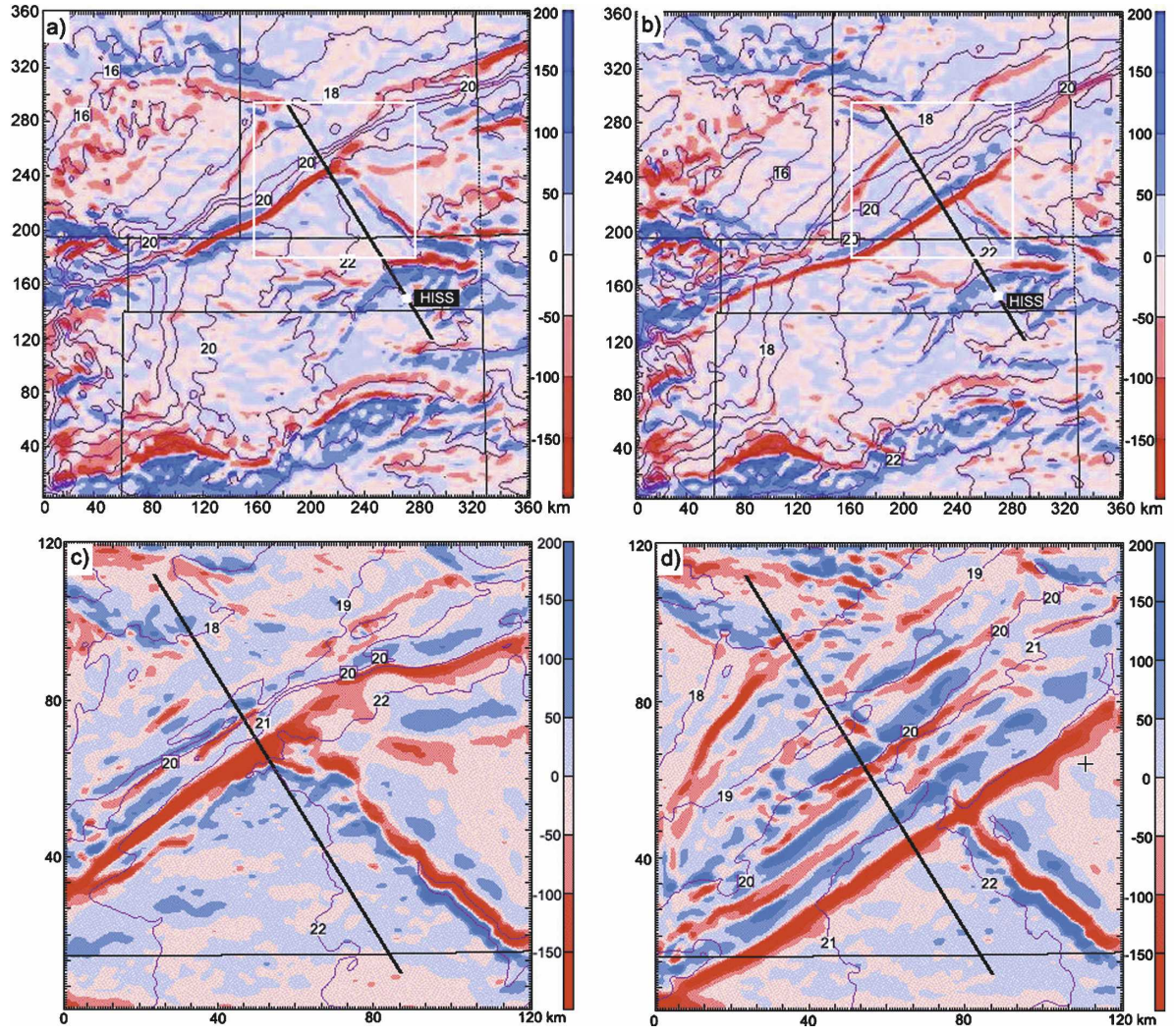

FIG. 19. MM5 model simulations of wind divergence (10^{-4} s^{-1}, blue: divergence, red: convergence) and isotherms (1°C intervals) at the surface from (a) 2.0-km-resolution model at 0800 UTC, (b) 2.0-km-resolution model at 0900 UTC, (c) 0.7-km-resolution model at 0800 UTC, and (d) 0.7-km-resolution model at 0900 UTC. The white box in (a) and (b) depicts region of nested 0.7-km model domains. Black line segments in (c) and (d) indicate positions of cross-sectional lines for both larger-scale and nested grid domains shown in Figs. 20–22. Bore front is identifiable as the northeast–southwest-oriented thin line of coupled convergence–divergence. Solitary wave train following in its wake develops in the nested model simulation. Terrain features or convection force other details in the divergence field.

taken at this point at the surface showing 2 g kg^{-1} decrease in a 2-h period (Fig. 22d). This particular detail is quite consistent with what was seen at RUST and similar stations during the active phase of bore B (Fig. 13b). Additionally present is the sudden moistening aloft resulting from the bore and subsequent solitary wave lifting, a feature similar to that discussed earlier (e.g., Fig. 18).

The MRI turbulence sensor on the UWKA (Xia 2001) provides supporting evidence for the model simulations of TKE and mixing processes. According to the Kolmogoroff similarity theory, the TKE within the inertial subrange (isr) is

$$\text{TKE} = C \int_{\text{isr}} \varepsilon^{2/3} k^{-5/3}\, dk, \tag{4}$$

where ε is the eddy dissipation rate (m^2 s^{-3}), k is the wavenumber, and C is a constant. The TKE (actually, $\varepsilon^{2/3}$) as measured by the MRI turbulence sensor is shown in Fig. 23a from three flight legs: the 1850-m leg, discussed earlier, that was flown through the bore front; a 240-m leg flown on a return leg toward the southeast; and a third leg made at 1410 m AGL. The locations of the flight legs relative to the bore front and the solitary waves are depicted in Figs. 23b and 23c. Note the parallel bands of reflectivity behind the bore front (high-

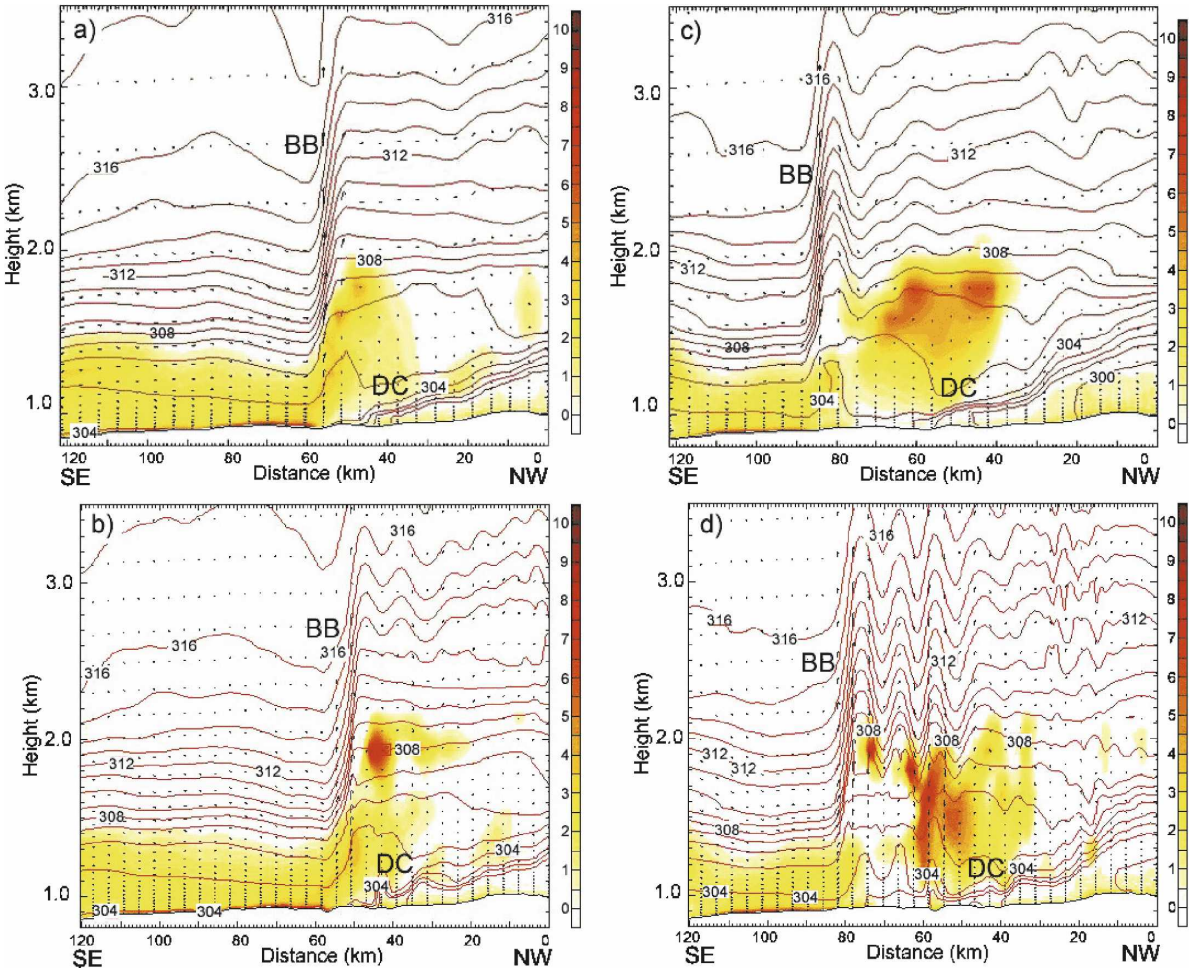

FIG. 20. Simulated potential temperature (1-K isentropes), TKE (color-fill, J kg^{-1}), and two-dimensional vertical circulation fields at (a) 0800 UTC from 2.0-km-resolution model, (b) 0800 UTC from 0.7-km-resolution model, (c) 0900 UTC from 2.0-km-resolution model, and (d) 0900 UTC from 0.7-km-resolution model. Cross section for both models is the same (cf. Figs. 19c,d). Panels have been rotated such that northwest (southeast) is to the right (left), in order to make comparison with the remote sensing systems more direct. Bore/soliton B (BB) evolves from, and propagates ahead of, density current (DC) in the simulation.

lighted by the black line in Fig. 23c). These are indicative of solitary waves. Turbulence is minimal at 1850 m AGL, whereas high values of TKE are encountered at 240 m AGL behind the bore in association with the solitary waves. The TKE peaks display an average period of 111 s, corresponding to a horizontal wavelength of 8.1 km given the ground speed of the aircraft minus the bore propagation speed, which agrees very well with the observed solitary wave scale. These data corroborate the model predictions showing negligible TKE within the solitary waves and strong TKE generation beneath each of the solitary waves.

6. Predictions from hydraulic theory

In this section, we use hydraulic theory to support our conjecture that the observed phenomena were bores. In addition, we draw comparisons regarding the horizontal wavelength of the solitary waves to the theory of Crook (1984) for a two-layer fluid, which is an extension of the theory of Benjamin and Lighthill (1954) for an undular bore on a free surface.

According to Rottman and Simpson (1989), bore propagation speed (C_{bore}) depends upon its depth (d_b), the inversion layer depth (h_0), and the long gravity wave speed (C_{gw}):

$$C_{\text{bore}}/C_{\text{gw}} = [0.5(d_b/h_0)(1 + d_b/h_0)]^{1/2}. \quad (5)$$

The long (or shallow water) wave speed is a function of the observed inversion depth and buoyancy frequency. Bore depth is a function of two parameters—the ratio of the density current speed to the gravity wave speed ($C_{\text{dc}}/C_{\text{gw}}$), and the density current depth (d_{dc}) normal-

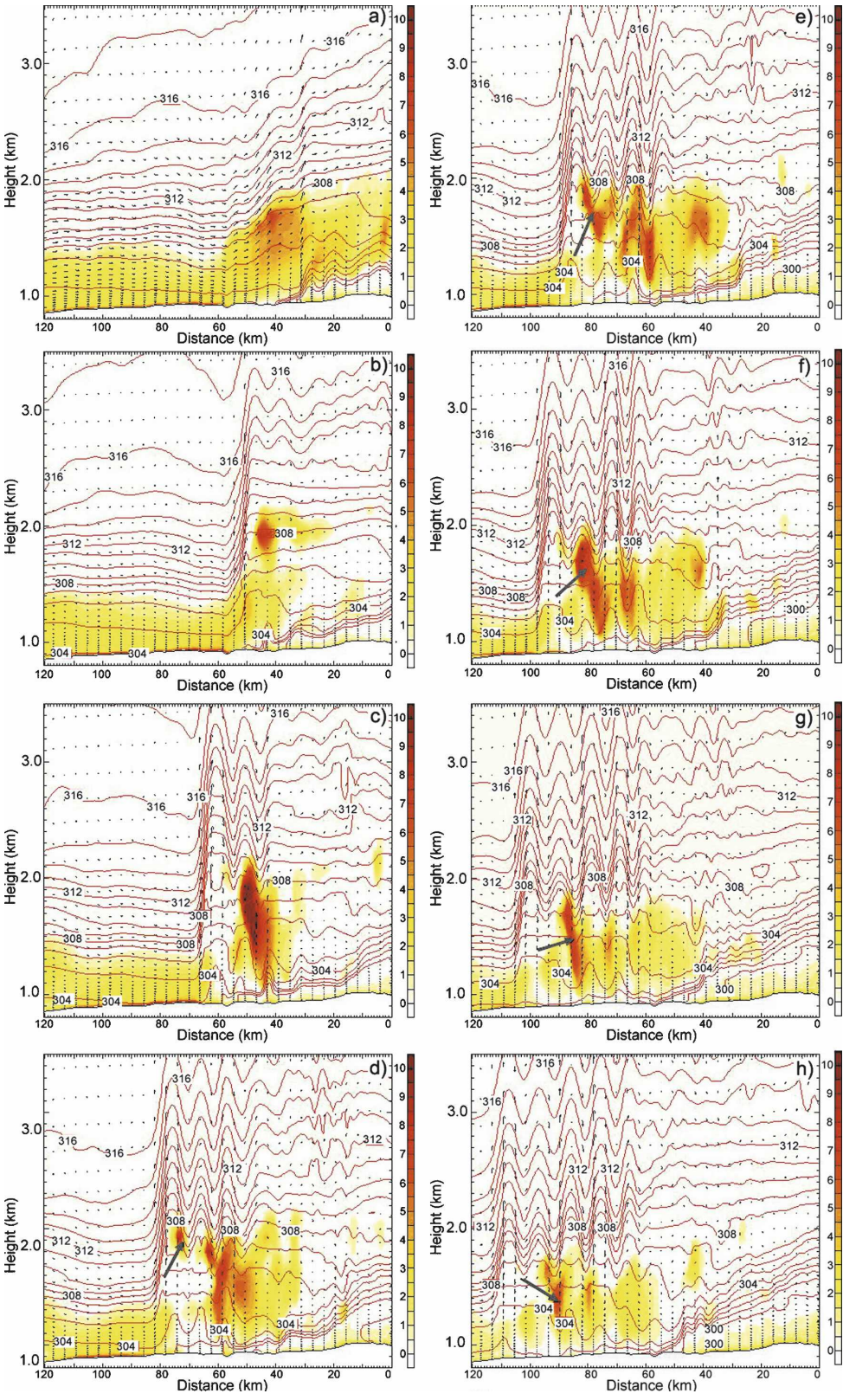

FIG. 21. Simulated potential temperature (1-K isentropes), TKE (color-fill; J kg^{-1}), and two-dimensional vertical circulation fields at (a) 0730, (b) 0800, (c) 0830, (d) 0900, (e) 0915, (f) 0930, (g) 0945, and (h) 1000 UTC from 0.7-km-resolution MM5 model run showing evolution from a density current [(a)] to a bore [(b)] and then to an amplitude-ordered soliton. Cross-section location is depicted in Figs. 19c,d. Arrow highlights a TKE feature discussed in the text.

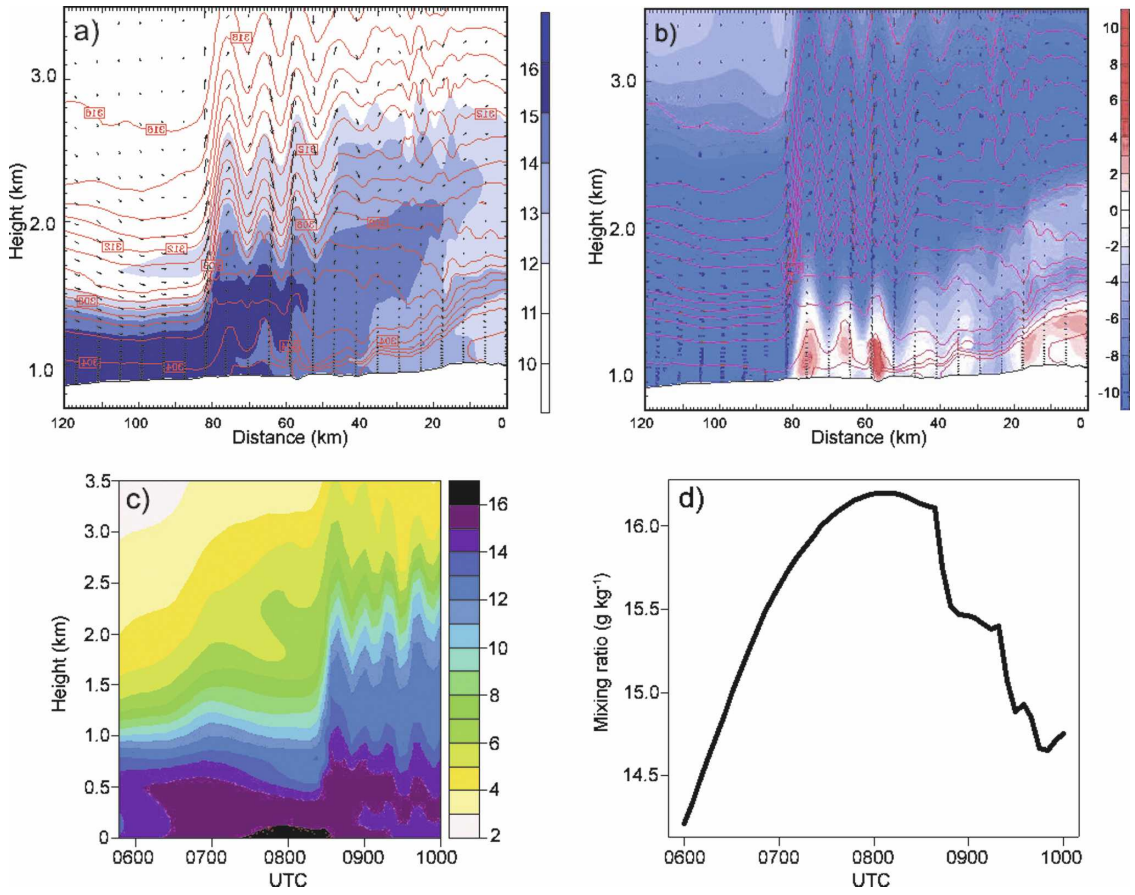

FIG. 22. MM5 0.7-km forecast for 0900 UTC of (a) mixing ratio (g kg^{-1}; color-fill) and potential temperature (1-K isentropes) along cross-section path in Fig. 19d, (b) bore-relative wind component (flow toward the bore from the southeast is in blue, and flow toward the bore from the northwest is in red; m s^{-1}) and isentropes, (c) time–height cross section of mixing ratio (g kg^{-1}) at the point where the bore front intersects the cross section at 0900 UTC (Fig. 19d), and (d) temporal variation in surface mixing ratio variations (g kg^{-1}) at the same point.

ized by the inversion depth (h_0). According to Koch et al. (1991),

$$d_{\rm dc} = \frac{\theta_{vc}\Delta p}{\rho_w g[(p_c/p_w)\theta_{vw} - \theta_{vc}]} \cong \left(\frac{C_{\rm dc}}{\rm Fr}\right)^2 \left(\frac{\theta_v}{g\Delta\theta_v}\right), \quad (6a)$$

$$C_{\rm dc} = {\rm Fr}\left(\frac{\Delta p}{\rho_w}\right)^{1/2} \approx {\rm Fr}\left(g d_{\rm dc}\frac{\Delta\theta_v}{\theta_v}\right)^{1/2}, \quad \text{and} \quad (6b)$$

$$C_{\rm gw} = \sqrt{g\Delta\theta_v(h_0/\theta_v)}, \quad (6c)$$

where θ_{vw} and θ_{vc} are the virtual potential temperatures in the warm and cold air masses, respectively; $\Delta\theta_v$ is the temperature jump across the inversion layer; Fr is a representative Froude number (arbitrarily assumed to be 0.95); and Δp represents the hydrostatic portion of the pressure jump at the head of the density current. Koch and Clark (1999, see their Table 3) applied four alternative predictions for bore speed to account for such factors as finite fluid depth, an extremely shallow stable layer, and the need to restrict energy loss to the neutral layer above the SBL waveguide (Klemp et al. 1997). In the comparisons with observations here, we use the average of all four theoretical predictions.

The predictions for density current speed and depth, bore propagation speed and depth, and the horizontal wavelength of the solitary waves are shown in Table 2 using input parameter values shown in Table 1. One conclusion drawn from these computations is that the bore depths observed by FM-CW, MAPR, UWKA, and SRL are within 300 m of the predicted values (i.e., within the observational error estimates). In addition, the observed bore speeds (9.8 and 10.2 m s^{-1}, respectively, for bores A and B) fall within the standard deviation of the various theoretical estimates. These comparisons with theory provide strong support for our contention that the observed phenomena were bores.

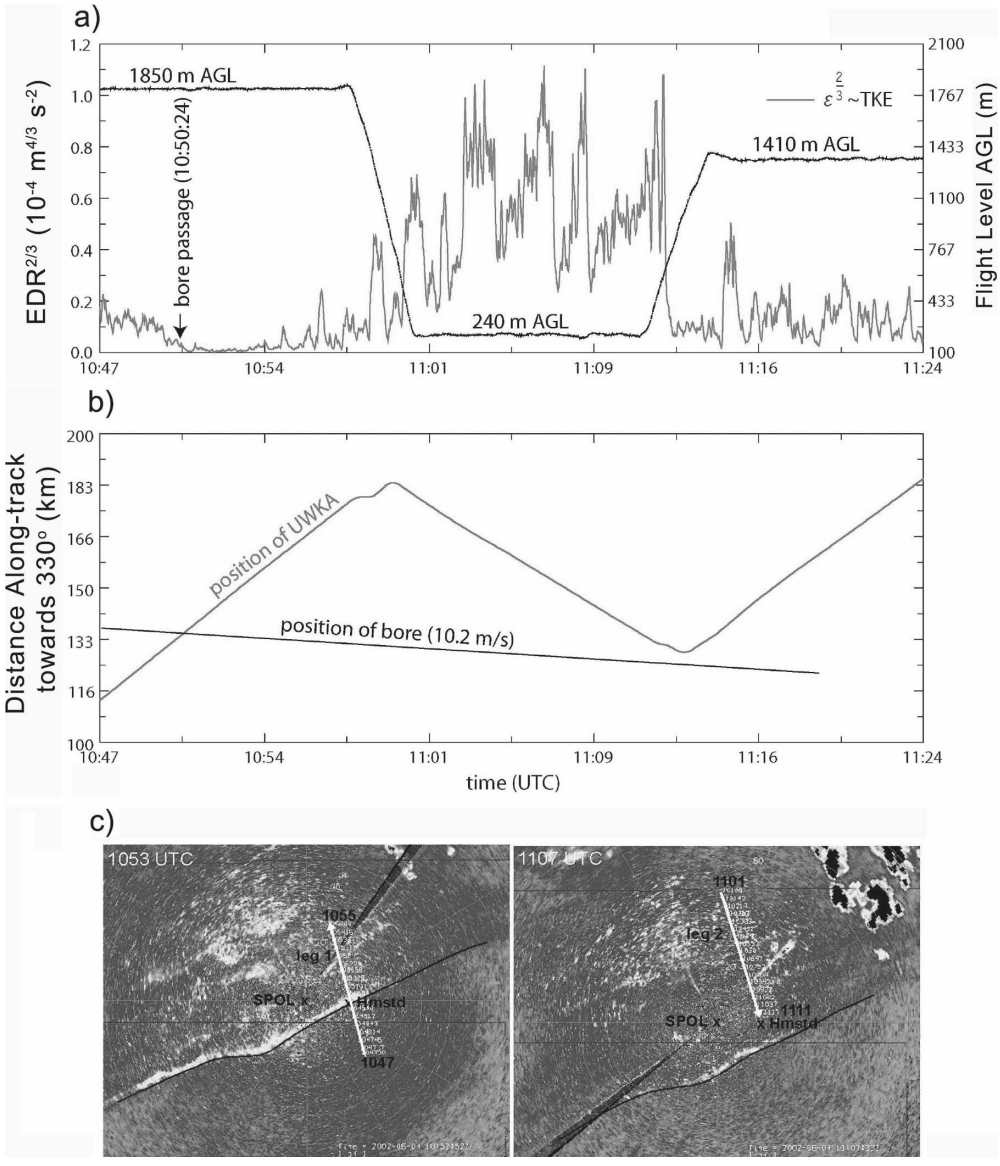

FIG. 23. Turbulence detected by UWKA: (a) $\varepsilon^{2/3}$ (10^{-4} m$^{4/3}$ s^{-2}; gray), where ε (m^2 s^{-3}) are the eddy dissipation rate (EDR) measurements taken by MRI sensor on flight legs for 1047–1124 UTC, and flight level (m AGL; black lines), (b) distance of aircraft relative to bore front location, and (c) paths of aircraft for 1850 m AGL leg (left; 1047–1055 UTC) and 240 m AGL leg (right; 1101–1111 UTC) superimposed on S-Pol reflectivity imagery.

The solitary wave predictions for horizontal wavelength are excellent for bore A, but not for bore B, because of the greater uncertainty regarding the inversion layer height in the latter case. The observed and predicted bore strengths all lie in the range of 1.73–2.20, which falls at or just below the lower end of values for which laboratory experiments indicate some mixing occurs behind the bore head (Rottman and Simpson 1989). The remote sensing observations discussed here qualitatively support those laboratory results.

7. Conclusions

The structure and dynamics of two bores that were generated during the early morning hours of 4 June 2002 and their evolution into an amplitude-ordered train of solitary waves derived from synthesis of the observations, numerical model simulations, and hydraulic theory have shed light on the entrainment and mixing processes associated with these phenomena. Detailed vertical structure and characteristics of these

TABLE 1. Input parameter values for prediction of bore propagation speed and depth from hydraulic theory. The source of data for determining values for the bores is shown in parentheses under "Data source or method of calculation."

Symbol	Parameter	Units	Bore A	Bore B	Data source or method of calculation
H	Tropopause height	km	12.2	10.8	0401 (1045) UTC Homestead soundings
d_b	Bore depth	km	1.30	2.30	FM-CW and MAPR (bore A), MAPR–UWKA–SRL (bore B)
h_0	Inversion depth	km	0.75	1.10	0401 (1045) UTC soundings (Fig. 10) + SRL for bore B
C_b	Bore propagation speed	m s^{-1}	9.8	10.2	Isochrone analyses of S-Pol fine lines (Figs. 14a, 15a)
$\Delta\theta$	Inversion strength	K	8.0	6.0	0401 (1045) UTC Homestead soundings (Fig. 10)
U	Mean head wind	m s^{-1}	17.0	17.5	0401 (1045) UTC Homestead soundings using C_b values
$\Delta\theta$	Density current cooling	K	5.5	7.6	Temperature drop at source of pressure jump (Figs. 14c, 15c)
C_{dc}	Density current speed	m s^{-1}	21.3	10.0	Isochrone analyses of S-Pol fine lines and pressure jump lines
Δp	Pressure jump	hPa	2.8	2.2	Value of pressure jump in density current region (Figs. 14b, 15b)
λ	Horizontal wavelength	km	15.8	8.3	Product of solitary wave speed (e.g., Fig. 7) and periodicity in FM-CW, MAPR, and UWKA data

phenomena were obtained using an unprecedented set of ground-based remote sensing systems and aircraft observations for study of bores and solitons. We believe this is also the first attempt to simulate details of observed solitary wave characteristics (horizontal wavelength, wave amplitude, phase speed, and structure) associated with a bore generated by moist convection with a numerical weather prediction model initialized using real data. Another original contribution of this study is its quantitative examination of the mixing processes associated with the life cycle of bores from inception to dissipation.

Despite the fact that both bores were in their dissipating stage when they passed over the Homestead observing site, the FM-CW, MAPR, HARLIE, and SRL systems all showed that the antecedent nocturnal inversion depth was nearly doubled by the passage of the bore. HARLIE showed that aerosols were wafted throughout an even deeper depth of the atmosphere by mixing associated with the solitary waves. The UW King Air aircraft and ground-based AERI data showed that the bores cooled and moistened the atmosphere aloft due to adiabatic lifting. Bore passage resulted in dramatic destabilization due to this moistening, plus lifting and weakening of the capping inversion, thereby making the atmosphere much more conducive to convective initiation than beforehand.

Detailed mesonet observations showed the following sequence of events at the surface: a strong pressure jump produced by cooling associated with the initial density current, followed by warming downstream of the pressure jump region due to downward mixing of air with higher potential temperature from above the inversion, and finally, strong refractivity decreases caused by a rapid drop in water vapor mixing ratio. However, by the time the bores had progressed to the Homestead facility, the drying signatures had vanished and, in some cases, been replaced by surface moistening, as the bores were dissipating. The AERI data at Homestead indicated that the bores produced pronounced *increases* of refractivity over the lowest 2 km associated with sudden increases of mixing ratio. It was conjectured that in the absence of vigorous mixing, the lifting by the bore head and solitary waves would only produce adiabatic cooling aloft and distribute the very moist air near the surface upward through a large depth without any surface drying. This conjecture was tested using numerical models.

Numerical simulations made from 2-km- and nested 0.7-km-resolution model runs both produced a bore

TABLE 2. Predicted bore propagation speed and depth from hydraulic theory using observed input parameter values in Table 1.

Symbol	Parameter	Units	Bore A	Bore B	Data source or method of calculation
d_b/h_0	Bore strength	—	1.73	2.09	Simple ratio
d_{dc}	Density current depth	km	1.42	0.94	Equation (6a) (first term)
d_{dc}/h_0	Normalized density current depth	—	1.89	0.72	Simple ratio
C_{dc}	Density current speed	m s^{-1}	16.8	16.6	Equation (6b) (second term)
C_{gw}	Gravity wave speed	m s^{-1}	13.7	14.4	Equation (6c)
C_{dc}/C_{gw}	Froude number	—	1.23	1.15	Simple ratio
d_b/h_0	Predicted bore strength	—	2.2	2.0	Koch and Clark (1999, Table 3)
d_b	Predicted bore depth	km	1.65	2.20	Product of predicted d_b/h_0 and observed h_0
C_b	Ground-relative bore speed	m s^{-1}	9.2 ± 0.8	11.3 ± 2.0	Predicted bore speed minus U
λ	Predicted horizontal wavelength	km	15.8	25.3	Crook (1984)

that corresponded well in timing and location to observed bore B, though neither was able to produce anything like bore A. These results were sensitive neither to model grid resolution, nor to the choice of PBL schemes tested. However, only the higher resolution model was able to produce a solitary wave train with characteristics similar to those observed. Turbulent kinetic energy was produced immediately to the rear of the bore head, and then advected rearward and distorted by the closed circulations associated with each of the solitary waves, with the result being strong turbulence and mixing in local regions under the waves. The mixing induced by the waves entrained air from above the inversion and transported this dry air throughout the PBL, resulting in a reduction of 2 g kg^{-1} at the surface. This process occurred during the active period of the bore and soliton in the model, and was substantiated by UWKA aircraft measurements of turbulence.

This study shows that it is possible for NWP models to predict bores and solitons, and to be used as research tools, in combination with remote sensing systems, to understand the dynamics of these phenomena. However, the value of the model depends upon whether it can skillfully forecast observed precipitation patterns, given the sensitivity of the density current and bore occurrence to this factor. Other necessary ingredients for successful numerical simulation include the proper simulation of the waveguide, such as a frontal system acting as a horizontal delimiter, and the strength of the low-level jet, which acts as an important mechanism for trapping vertical wave energy propagation.

Acknowledgments. We express our appreciation to the University Corporation for Atmospheric Research/Joint Office for Science Support (UCAR/JOSS) for creating the very useful composites of 1-, 5-, and 60-min surface mesonet datasets. Rita Roberts (NCAR) helped create the surface and radar composite analyses. Discussions with Crystal Pettet (NCAR) about the refractivity changes derived from AERI, S-Pol, and the mesonet stations were helpful. Jeff Keeler and Tammy Weckwerth (NCAR) offered assistance in the interpretation of the FM-CW noise problems. Bill Brown (NCAR) provided information concerning the MAPR data, and Dave Whiteman and Belay Demoz (NASA) did likewise with the SRL data. Geary Schwemmer (NASA) and Annie Reiser (NOAA) reviewed this manuscript and provided useful comments.

REFERENCES

Arya, S. P., 2000: Atmospheric boundary layers and turbulence. *Mesoscale Atmospheric Dispersion,* Z. Boybeyi, Ed., WIT Press, 121–170.

Battan, L. J., 1973: *Radar Observation of the Atmosphere.* University of Chicago Press, 324 pp.

Benjamin, T. B., and M. J. Lighthill, 1954: On cnoidal waves and bores. *Proc. Roy. Soc. London,* **224,** 448–460.

Burk, S. D., and W. T. Thompson, 1989: A vertically nested regional numerical weather prediction model with second-order closure physics. *Mon. Wea. Rev.,* **117,** 2305–2324.

Christie, D. R., K. J. Muirhead, and A. L. Hales, 1979: Intrusive density flows in the lower troposphere: A source of atmospheric solitons. *J. Geophys. Res.,* **84,** 4959–4970.

Cohn, S. A., W. O. J. Brown, C. L. Martin, M. E. Susedik, G. Maclean, and D. B. Parsons, 2001: Clear air boundary layer spaced antenna wind measurement with the Multiple Antenna Profiler (MAPR). *Ann. Geophys.,* **19,** 845–854.

Crook, N. A., 1984: A numerical and analytical study of atmospheric undular bores. Ph.D. thesis, Imperial College, University of London, 128 pp.

——, 1988: Trapping of low-level internal gravity waves. *J. Atmos. Sci.,* **45,** 1533–1541.

Doviak, R. J., and R. Ge, 1984: An atmospheric solitary gust observed with a Doppler radar, a tall tower and a surface network. *J. Atmos. Sci.,* **41,** 2559–2573.

Droegemeier, K. K., and R. B. Wilhelmson, 1985: Three-dimensional numerical modeling of convection produced by interacting thunderstorm outflows. Part I: Control simulation and low-level moisture variations. *J. Atmos. Sci.,* **42,** 2381–2403.

Fabry, F., C. Frush, I. Zawadzki, and A. Kilambi, 1997: On the extraction of near-surface index of refraction using radar phase measurements from ground targets. *J. Atmos. Oceanic Technol.,* **14,** 978–987.

Fedorovich, E., R. Rotunno, and B. Stevens, Eds., 2004: *Atmospheric Turbulence and Mesoscale Meteorology: Scientific Research Inspired by Doug Lilly.* Cambridge University Press, 280 pp.

Feltz, W. F., W. L. Smith, R. O. Knuteson, H. E. Revercomb, H. M. Woolf, and H. B. Howell, 1998: Meteorological applications of temperature and water vapor retrievals from the ground-based Atmospheric Emitted Radiance Interferometer (AERI). *J. Appl. Meteor.,* **37,** 857–875.

——, D. J. Posselt, J. R. Mecikalski, G. S. Wade, and T. J. Schmit, 2003a: Rapid boundary layer water vapor transitions. *Bull. Amer. Meteor. Soc.,* **84,** 29–30.

——, W. L. Smith, H. B. Howell, R. O. Knuteson, H. Woolf, and H. E. Revercomb, 2003b: Near-continuous profiling of temperature, moisture, and atmospheric stability using the Atmospheric Emitted Radiance Interferometer (AERI). *J. Appl. Meteor.,* **42,** 584–597.

Fulton, R., D. S. Zrnić, and R. J. Doviak, 1990: Initiation of a solitary wave family in the demise of a nocturnal thunderstorm density current. *J. Atmos. Sci.,* **47,** 319–337.

Geerts, B., R. Damiani, and S. Haimov, 2006: Finescale vertical structure of a cold front as revealed by an airborne Doppler radar. *Mon. Wea. Rev.,* **134,** 251–271.

Grell, G. A., and D. Dévényi, 2002: A generalized approach to parameterizing convection combining ensemble and data assimilation techniques. *Geophys. Res. Lett.,* **29,** 1693, doi:10.1029/2002GL015311.

Haase, S. P., 1991: Numerical simulation of the bore-like cold front of 8 October 1987 in southern Germany. *Tellus,* **43A,** 97–105.

——, and R. K. Smith, 1989a: The numerical simulation of atmo-

spheric gravity currents. Part I: Neutrally-stable environments. *Geophys. Astrophys. Fluid Dyn.,* **46,** 1–33.

——, and ——, 1989b: The numerical simulation of atmospheric gravity currents. Part II: Environments with stable layers. *Geophys. Astrophys. Fluid Dyn.,* **46,** 35–51.

İnce, T., S. J. Frasier, A. Muschinski, and A. L. Pazmany, 2003: An S-band frequency-modulated continuous-wave boundary layer profiler: Description and initial results. *Radio Sci.,* **38,** 1072, doi:10.1029/2002RS002753.

Janjić, Z. I., 1994: The step-mountain Eta coordinate model: Further developments of the convection, viscous sublayer, and turbulence closure schemes. *Mon. Wea. Rev.,* **122,** 927–945.

Jin, Y., S. E. Koch, Y.-L. Lin, F. M. Ralph, and C. Chen, 1996: Numerical simulations of an observed gravity current and gravity waves in an environment characterized by complex stratification and shear. *J. Atmos. Sci.,* **53,** 3570–3588.

Karyampudi, V. M., S. E. Koch, C. Chen, J. W. Rottman, and M. L. Kaplan, 1995: The influence of the Rocky Mountains on the 13–14 April 1986 severe weather outbreak. Part II: Evolution of a prefrontal bore and its role in triggering a squall line. *Mon. Wea. Rev.,* **123,** 1423–1446.

Klemp, J. B., R. Rotunno, and W. C. Skamarock, 1997: On the propagation of internal bores. *J. Fluid Mech.,* **331,** 81–106.

Knuteson, R. O., and Coauthors, 2004a: Atmospheric Emitted Radiance Interferometer. Part I: Instrument design. *J. Atmos. Oceanic Technol.,* **21,** 1763–1776.

——, and Coauthors, 2004b: Atmospheric Emitted Radiance Interferometer. Part II: Instrument performance. *J. Atmos. Oceanic Technol.,* **21,** 1777–1789.

Koch, S. E., and W. L. Clark, 1999: A nonclassical cold front observed during COPS-91: Frontal structure and the process of severe storm initiation. *J. Atmos. Sci.,* **56,** 2862–2890.

——, P. B. Dorian, R. Ferrare, S. H. Melfi, W. C. Skillman, and D. Whiteman, 1991: Structure of an internal bore and dissipating gravity current as revealed by Raman lidar. *Mon. Wea. Rev.,* **119,** 857–887.

LeMone, M. A., G. M. Barnes, J. C. Fankhauser, and L. F. Tarleton, 1988: Perturbation pressure fields measured by aircraft around the cloud-base updraft of deep convective clouds. *Mon. Wea. Rev.,* **116,** 313–327.

Lutz, J., P. Johnson, B. Lewis, E. Loew, M. Randall, and J. VanAndel, 1995: NCAR's S-Pol: Portable polarimetric S-band radar. Preprints, *Ninth Symp. on Meteorological Observations and Instrumentation,* Charlotte, NC, Amer. Meteor. Soc., 408–410.

Manobianco, J., and P. A. Nutter, 1999: Evaluation of the 29-km Eta model. Part II: Subjective verification over Florida. *Wea. Forecasting,* **14,** 18–37.

Mlawer, E. J., S. J. Taubman, P. D. Brown, M. J. Iacono, and S. A. Clough, 1997: Radiative transfer for inhomogeneous atmospheres: RRTM, a validated correlated-*k* model for the longwave. *J. Geophys. Res.,* **102,** 16 663–16 682.

Moran, M. D., 2000: Basic aspects of mesoscale atmospheric dispersion. *Mesoscale Atmospheric Dispersion,* Z. Boybeyi, Ed., WIT Press, 27–119.

Mueller, C. K., and R. E. Carbone, 1987: Dynamics of a thunderstorm outflow. *J. Atmos. Sci.,* **44,** 1879–1898.

Reisner, J., R. M. Rasmussen, and R. T. Bruintjes, 1998: Explicit forecasting of supercooled liquid water in winter storms using the MM5 mesoscale model. *Quart. J. Roy. Meteor. Soc.,* **124,** 1071–1107.

Rottman, J. W., and J. E. Simpson, 1989: The formation of internal bores in the atmosphere: A laboratory model. *Quart. J. Roy. Meteor. Soc.,* **115,** 941–963.

Schwemmer, G. K., T. D. Wilkerson, and D. V. Guerra, 1998: Compact scanning lidar systems using holographic optics. *Optical Remote Sensing for Industry and Environmental Monitoring,* U. N. Singh, H. Hu, and G. Wang, Eds., International Society for Optical Engineering (SPIE Proceedings, Vol. 3504), 51–59.

Simpson, J. E., 1987: *Gravity Currents: In the Environment and the Laboratory.* Halsted Press, 244 pp.

Skyllingstad, E. D., 1991: Critical layer effects on atmospheric solitary and cnoidal waves. *J. Atmos. Sci.,* **48,** 1613–1624.

Smirnova, T. G., J. M. Brown, S. G. Benjamin, and D. Kim, 2000: Parameterization of cold-season processes in the MAPS land-surface scheme. *J. Geophys. Res.,* **105,** 4077–4086.

Smith, R. K., 1988: Travelling waves and bores in the lower atmosphere: The 'Morning Glory' and related phenomena. *Earth-Sci. Rev.,* **25,** 267–290.

Thomsen, G. L., and R. K. Smith, 2006: Simulations of low-level convergence lines over north-eastern Australia. *Quart. J. Roy. Meteor. Soc.,* **132,** 691–707.

Weckwerth, T. M., and Coauthors, 2004: An overview of the International H_2O Project (IHOP_2002) and some preliminary highlights. *Bull. Amer. Meteor. Soc.,* **85,** 253–277.

——, C. R. Pettet, F. Fabry, S. Park, M. A. LeMone, and J. W. Wilson, 2005: Radar refractivity retrieval: Validation and application to short-term forecasting. *J. Appl. Meteor.,* **44,** 285–300.

Whiteman, D. N., and Coauthors, 2006a: Raman lidar measurements during the International H_2O Project. Part I: Instrumentation and analysis techniques. *J. Atmos. Oceanic Technol.,* **23,** 157–169.

——, and Coauthors, 2006b: Raman lidar measurements during the International H_2O Project. Part II: Case studies. *J. Atmos. Oceanic Technol.,* **23,** 170–183.

Wilson, J. W., and W. E. Schreiber, 1986: Initiation of convective storms at radar-observed boundary-layer convergence lines. *Mon. Wea. Rev.,* **114,** 2516–2536.

Xia, F., 2001: Evaluation of the MacReady turbulence sensor. M.S. thesis, Dept. of Atmospheric Science, University of Wyoming, 192 pp.

Xu, Q., 1992: Density currents in shear flows—A two-fluid model. *J. Atmos. Sci.,* **49,** 511–524.

Zhang, D., and R. A. Anthes, 1982: A high-resolution model of the planetary boundary layer—Sensitivity tests and comparisons with SESAME-79 data. *J. Appl. Meteor.,* **21,** 1594–1609.